Characterization of soil dust aerosol in China and its transport and distribution during 2001 ACE-Asia: 2. Model simulation and validation

S. L. Gong,[1,2] X. Y. Zhang,[2] T. L. Zhao,[3] I. G. McKendry,[4] D. A. Jaffe,[5] and N. M. Lu[6]

Received 7 June 2002; revised 20 November 2002; accepted 14 January 2003; published 2 May 2003.

[1] A size-segregated soil dust emission and transport model, Northern Aerosol Regional Climate Model (NARCM), was used to simulate the production and transport of Asian soil dust during the Aerosol Characterization Experiment-Asia (ACE-Asia) period from March to May 2001. The model is driven by the NCEP reanalyzed meteorology and has all the atmospheric aerosol physical processes of soil dust: production, transport, growth, coagulation, and dry and wet deposition. A Chinese soil texture map that infers the soil grain-size distribution with 12 categories was generated to drive the size-distributed soil dust emission scheme [*Alfaro et al.*, 1997; *Marticorena and Bergametti*, 1995]. The size distribution of vertical dust flux was derived from the observed surface dust-size distribution in the desert regions. Parameters applicable to the Asian deserts for the dust emission scheme are assessed. Model simulations were compared with ground-based measurements in East Asia and North America and with satellite measurements for the same period of time. The model captured most of the dust mobilization episodes during this period in China and reasonably simulated the concentrations in source regions and downwind areas from East China to western North America. About 252.8 Mt of soil dust below $d < 40$ μm was estimated to be emitted in the East Asian deserts between 1 March and 31 May 2001 with ~60% attributed to four major dust storms. The vertical dust loadings above 700 hPa correlate reasonably well with Total Ozone Mapping Spectrometer aerosol index (TOMS AI) observations. The sensitivity analysis of model performance to soil size distribution, water moisture, and meteorology was carried out with the observational data to establish the most appropriate parameters and conditions for the Chinese soil dust production and transport. *INDEX TERMS:* 0305 Atmospheric Composition and Structure: Aerosols and particles (0345, 4801); 0322 Atmospheric Composition and Structure: Constituent sources and sinks; 0368 Atmospheric Composition and Structure: Troposphere—constituent transport and chemistry; 3210 Mathematical Geophysics: Modeling; *KEYWORDS:* Asia, soil dust, observation, simulation, ACE-Asia

Citation: Gong, S. L., X. Y. Zhang, T. L. Zhao, I. G. McKendry, D. A. Jaffe, and N. M. Lu, Characterization of soil dust aerosol in China and its transport and distribution during 2001 ACE-Asia: 2. Model simulation and validation, *J. Geophys. Res.*, *108*(D9), 4262, doi:10.1029/2002JD002633, 2003.

1. Introduction

[2] Among the natural aerosol sources, soil dust is a major contributor to global aerosol mass load and optical thickness. Estimates of its global source strength range from 1000 to 5000 Mt/yr [*Duce*, 1995], with very high spatial and temporal variability. Dust uplifting occurs in a source region when the surface wind speed exceeds a threshold velocity, which is a function of surface roughness elements, grain size, and soil moisture [*Marticorena and Bergametti*, 1995; *Wang et al.*, 2000]. Fine soil particles that can be transported over large distances are released by saltating sand particles [e.g., *Gomes et al.*, 1990]. The transport of desert dust from Asia to the North Pacific atmosphere is well documented [*Duce et al.*, 1980; *Husar et al.*, 1997, 2001; *Uematsu et al.*, 1983] and results in a maximum in aerosol loading each spring. Over the Pacific, the concentration of species from anthropogenic sources in Asia was also found to be enhanced during spring [*Prospero and Savoie*, 1989] and has been documented to reach North America [*Jaffe et al.*, 1999].

[1]Air Quality Research Branch, Meteorological Service of Canada, Toronto, Ontario, Canada.
[2]State Key Laboratory of Loess and Quaternary Geology, Institute of Earth Environment, Chinese Academy of Sciences, Xian, China.
[3]Department of Chemical Engineering and Applied Chemistry, University of Toronto, Toronto, Ontario, Canada.
[4]Atmospheric Science Programme/Geography, University of British Columbia, Vancouver, British Columbia, Canada.
[5]University of Washington-Bothell, Bothell, Washington, USA.
[6]National Satellite and Meteorological Center, Chinese Meteorological Administration, Beijing, China.

0148-0227/03/2002JD002633$09.00

[3] The impact of soil dust from natural and anthropogenic sources on climate and air quality has been recognized at the global scale [*Sokolik and Toon*, 1996; *Tegen and Fung*, 1994]. However, the regional characteristics of soil dust production, transport, and removal processes are poorly understood. Increased dust emission and transport may have produced significant episodic regional warming of $\sim$5°C downwind of the major Asian dust source regions [*Overpeck et al.*, 1996]. Larger quantities of dust transported over the oceans can induce ocean cooling by reflecting solar radiation back to space. *Sokolik and Toon* [1996] showed that a dust-laden atmosphere with an average optical thickness of 0.5 would cause net radiative forcing of 20–40 W m^2 over arid regions and -5 to -15 W m^2 over the ocean. Less ocean warming compared with land areas close to the dust sources was also suggested from the climate simulations by *Overpeck et al.* [1996]. This contrasting impact of dust aerosols between continental source regions and oceans could alter the Asian winter monsoon circulation and have an influence on the dust emission in the source regions. In addition, the deposition of soil dust over oceans provides marine nutrients (e.g., iron) for phytoplankton [*Martin et al.*, 1994] and may regulate the production of DMS, which has a climatic impact itself [*Charlson et al.*, 1987].

[4] To accurately predict the impact of soil dust aerosols on climate, the spatial and temporal distribution of dust loading together with detailed physical and chemical properties (e.g., size distribution and composition) are required. Current global models do not adequately simulate the spatial and temporal distribution of soil dust in Asia due to their poor spatial resolution and inaccuracy of the dust source function. Furthermore, simulations have not been validated over Asian source regions. Regional dust transport models have shown similar limitations [*Song and Carmichael*, 2001; *Uno et al.*, 2001]. The lack of knowledge of detailed surface soil properties together with a dearth of observations in the source regions has been a major obstacle to better model prediction of soil dust emission strength, and hence dust loading downwind of Asian source regions [*Sokolik et al.*, 2001].

[5] During spring 2001, the intensive field phase for Aerosol Characterization Experiment-Asia (ACE-Asia) was conducted off the coast of China, Japan, and Korea. Within China, measurements of soil dust were also made to characterize the aerosol properties in that region and provide experimental data to compare with model simulations. In our companion paper, the surface measurements of soil dust in China during ACE-Asia are presented [*Zhang et al.*, 2003]. In this paper a regional climate model with a size-distributed active aerosol algorithm, northern aerosol regional climate model (NARCM), was used to simulate the production and transport of dust in eastern Asia and over the North Pacific Ocean during dust storms in spring 2001. The model is driven by National Centers for Environmental Prediction (NCEP) reanalyzed meteorology and has all atmospheric soil dust aerosol processes: production, transport, dry deposition, below-cloud scavenging, and an explicit microphysical cloud module to treat the aerosol-cloud interactions. A detailed soil texture data set [*Hseung*, 1984] and up-to-date desert distribution in China [*Chinese Academy of Sciences* (*CAS*), 1998] was obtained and used to drive the size-distributed dust emission module. In this paper, model simulations of the spatiotemporal distribution and trans-Pacific transport of the soil dust during spring 2001 are compared with observations. The size-distributed dust budgets that include emission fluxes and dry and wet deposition will follow in a separate paper.

2. Model Description and Input Data

[6] Aerosols are represented in the NARCM by a size-segregated prognostic equation in such a way that for aerosol particles with a dry size range (or section), *i*, the mass balance equation can be written as

$$\frac{\partial \chi_{ip}}{\partial t} = \left.\frac{\partial \chi_{ip}}{\partial t}\right|_{\text{transport}} + \left.\frac{\partial \chi_{ip}}{\partial t}\right|_{\text{sources}} + \left.\frac{\partial \chi_{ip}}{\partial t}\right|_{\text{clear air}} + \left.\frac{\partial \chi_{ip}}{\partial t}\right|_{\text{dry}} + \left.\frac{\partial \chi_{ip}}{\partial t}\right|_{\text{in-cloud}} + \left.\frac{\partial \chi_{ip}}{\partial t}\right|_{\text{below-clouds}}. \quad (1)$$

In equation (1), the rate of change of mixing ratio of dry particle mass constituent p in a size range, i, has been divided into components (or tendencies) for dynamics, sources, clear air, dry deposition, in-cloud and below-cloud processes. The transport includes resolved motion as well as subgrid turbulent diffusion and convection. The sources include (1) surface emission rate of both natural and anthropogenic aerosols, and (2) production of secondary aerosols (i.e., airborne aerosol mass produced by chemical transformation of their precursors). The latter, together with particle nucleation, condensation, and coagulation, contribute to the clear-air process. Dry deposition of gases and particles affects the "dry" tendency. Except for the transport and the source function of soil dust emission, the treatment of other atmospheric aerosol processes has been included in an aerosol module, Canadian aerosol module (CAM) and described in detail by *Gong et al.* [2003]. Consequently, this section will describe the treatment of transport and soil dust emission scheme.

2.1. Aerosol Transport

[7] The transport model that couples with CAM to simulate the soil dust distributions is the Canadian regional climate model (RCM) used in the NARCM project. RCM is a regional climate model that uses the physics package from the Canadian global climate model (GCM) and a semi-Lagrangian and semi-implicit transport scheme for dynamics and passive tracers [*Robert et al.*, 1985]. Simulations by NARCM can be conducted in two modes based on the meteorological boundary conditions. In climate mode, the simulation results from GCM are used as the lateral boundary conditions which reflect a climate mean. In the second mode, the observed or reanalyzed meteorological conditions in the region are used to drive the model as initial and boundary conditions that reflect a specific period of time. From the constraints in the lateral boundary, the meteorology inside the domain is developed by the model itself (with the exception for wind speed, which could be nudged to the observed or reanalyzed).

[8] Given the episodic nature of soil dust emission and transport, the second mode was adopted in this study. The NCEP reanalyzed meteorology for spring 2001 was used to drive the NARCM with a fully nudged wind speed every

6 hours (the rate at which NCEP updates its meteorology). This method ensures that wind speeds generated by the model match closely with the NCEP data. As it will be shown in section 2.2, the wind speed is a critical parameter to both production and transport of soil dust.

2.2. Soil Dust Source Function

[9] Production of soil dust aerosols depends on two factors: (1) surface wind speed, and (2) soil surface properties. It is generally recognized that soil dust particles are mobilized only for wind speed greater than a threshold value [*Marticorena and Bergametti*, 1995]. This threshold of wind speed depends on the minimum threshold friction velocity, u_t^*. In the current model, only suspension of particles with d < 40 μm is considered, as they are small enough to be transported by turbulent eddies and advection.

[10] For a smooth surface, the threshold friction velocity is given by *Marticorena and Bergametti* [1995]:

$$u_{tS}^*(r_s) = \begin{cases} \dfrac{0.129K}{\left(1.928\mathrm{Re}^{0.092}-1\right)^{0.5}} & 0.03 < \mathrm{Re} \le 10 \\ 0.129K\{1-0.0858\exp[-0.0617(\mathrm{Re}-10)]\} & \mathrm{Re} > 10 \end{cases}, \quad (2)$$

where

$$\mathrm{Re} = a(2r_s)^X + b, \quad a = 1331\,\mathrm{cm}^{-X}, \quad b = 0.38, \quad X = 1.56,$$

$$K = \left(\frac{2\rho_p g r_s}{\rho_a}\right)^{0.5}\left(1+\frac{0.006}{\rho_p g(2r_s)^{2.4}}\right)^{0.5},$$

ρ_p and ρ_a are the density of soil dust and air, respectively, g is the gravitational acceleration, and r_s is soil particle radius. Taking into account the effects of nonerodible elements in the grid by using a roughness length parameterization, *Marticorena and Bergametti* [1995] suggested the following correction to the threshold friction velocity:

$$u_{tR}^*(r_s) = u_{tS}^*\left\{1-\left[\frac{\ln(Z_m/z_{0S})}{\ln\left[0.35(10/z_{0S})^{0.8}\right]}\right]\right\}, \quad (3)$$

where Z_m (cm) is the initial roughness length of heterogeneous land covers and z_{0S} ($\sim 10^{-3}$ cm) is the local roughness length of the uncovered surface. The threshold friction velocity is also a function of soil moisture content, which has be parameterized [*Fécan et al.*, 1999] as

$$\frac{u_t^*}{u_{tR}^*} = \begin{cases} 1 & \text{for} \quad w < w' \\ [1+1.21(w-w')0.68]^{0.5} & \text{for} \quad w > w' \end{cases}, \quad (4)$$

where w and w' are the ambient and threshold volumetric soil moisture with $w' = 0.0014(\%\mathrm{clay})^2 + 0.17(\%\mathrm{clay})$.

[11] The horizontal mass flux with a radius interval dr_s, representing the quantity of material in movement in the saltation layer, is related to the critical friction velocity by *Marticorena and Bergametti* [1995] as

$$dF_h(r_s) = E\frac{\rho_a}{g}u^{*3}(1+R)\left(1-R^2\right)S_{\mathrm{rel}}(r_S)dr_s, \quad (5)$$

where E is the ratio of erodible to total surface, $S_{\mathrm{rel}}(r_s)$ is the relative surface covered by particles of radii from r_s to $r_s + dr_s$, $\int S_{\mathrm{rel}}(r_s)dr_s = 1$ for all sizes of particles, and $R = u_t^*/u^*$. Computation of S_{rel} requires the soil mass size distribution for the source regions as described in section 2.3.1.

[12] Horizontal flux cannot be directly used in the model. The vertical flux and its size distribution are required. In the saltation and sandblasting process, the fine particles released either from saltating aggregates or from the surface depend on the individual kinetic energy [*Alfaro et al.*, 1998]:

$$e_c = \rho_p\pi/12(2r_s)^3(20u^*)^2. \quad (6)$$

Three lognormal population distributions for the particles released by sandblasting from the saltating aggregates were suggested [*Alfaro et al.*, 1998]. The mass median diameters (d_i), standard deviations (σ_i), and binding energies (e_i) of these three populations (i = 1, 2, 3) are introduced in NARCM by considering the soil features in Asia, especially in China, and source region dust size-distribution measurements [*Zhang et al.*, 2003]. The binding energies (e_i) in NARCM for the three soil dust distributions were calculated from the fraction (p_i) of the kinetic energy (e_c) of individual saltating aggregate [*Alfaro et al.*, 1997].

[13] The kinetic energy (vertical) flux $dF_{\mathrm{kin}}(r_s)$ of saltating aggregates with radii from r_s to $r_s + dr_s$ is proportional to the corresponding horizontal mass flux [*Alfaro et al.*, 1997; *Alfaro and Gomes*, 2001]:

$$dF_{kin}(r_s) = \beta dF_h(r_s), \quad (7)$$

with β = 16,300 cm s^{-2}. By defining $p_i = p_i(r_s)$ [*Alfaro et al.*, 1997], the fraction of $dF_{\mathrm{kin}}(r_s)$ that is available to release particles of the ith aerosol population is $p_i\beta dF_h(r_s)$ and its number flux $dN_i(r_s) = \beta dF_h(r_s)p_i/e_i$. Consequently, the total number (N_i) and mass fluxes ($F_{\mathrm{soil},i}$) of each population are

$$N_i = \frac{\beta}{e_i}\int_{r_S} p_i dF_h(r_s) \quad (8)$$

$$F_{\mathrm{soil},i} = \left(\pi\rho_p d_i^3/6\right)N_i. \quad (9)$$

[14] The total dust flux that represents fine transportable particles (d_i < 40 μm) as the dust source strength is

$$F_{SD} = \left(\sum_{i=1}^{3} F_{\mathrm{soil},i}\right). \quad (10)$$

[15] Parameters used in this dust emission scheme (equations (2)–(10)) depend strongly on geographic locations. Some of the parameters have been only verified in Saharan deserts [*Marticorena et al.*, 1997] or wind tunnel experi-

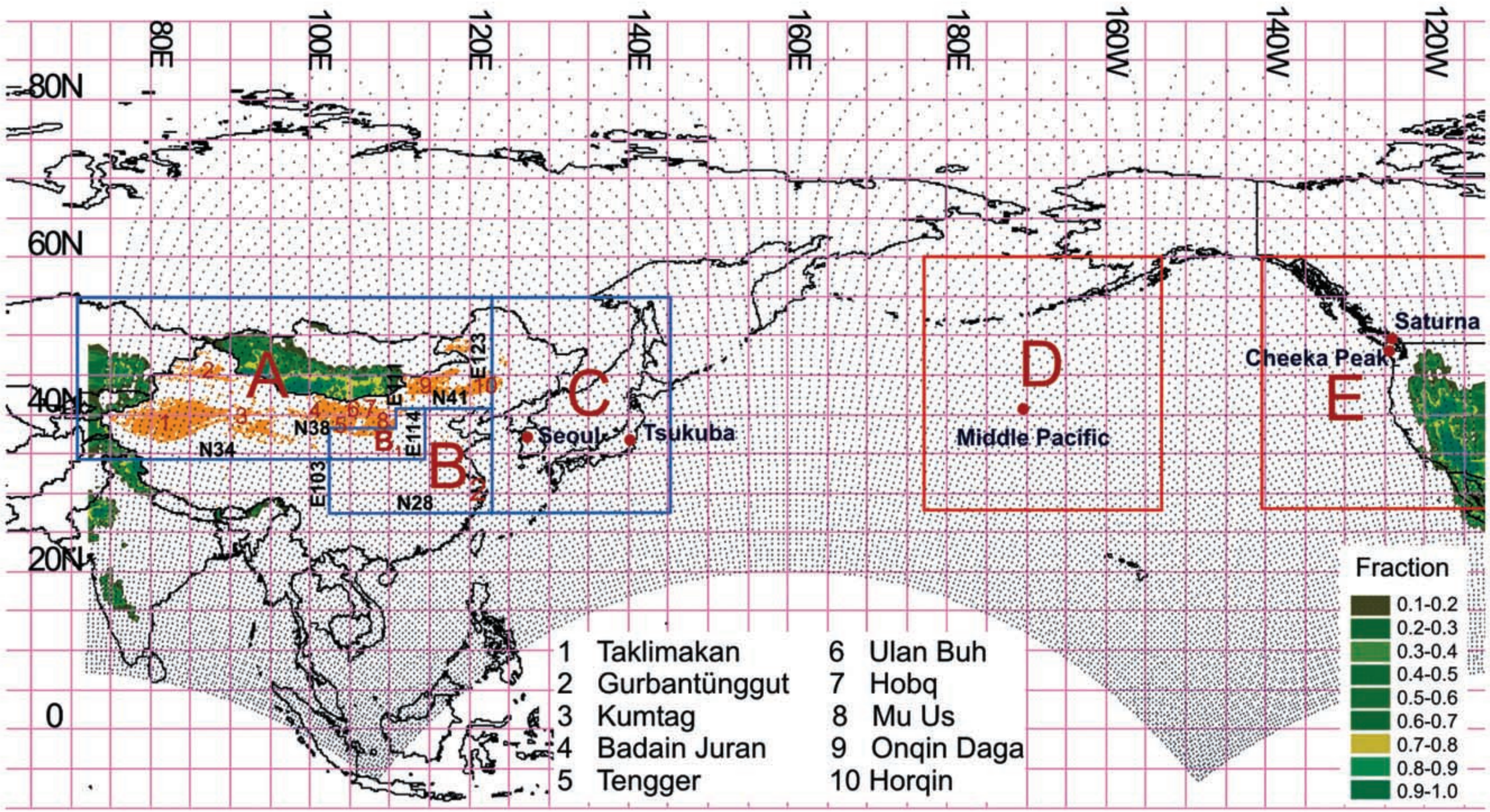

Figure 1. Desert distributions in China and model simulation domain. The deserts outside China are expressed as percentages in a grid and shown as contours.

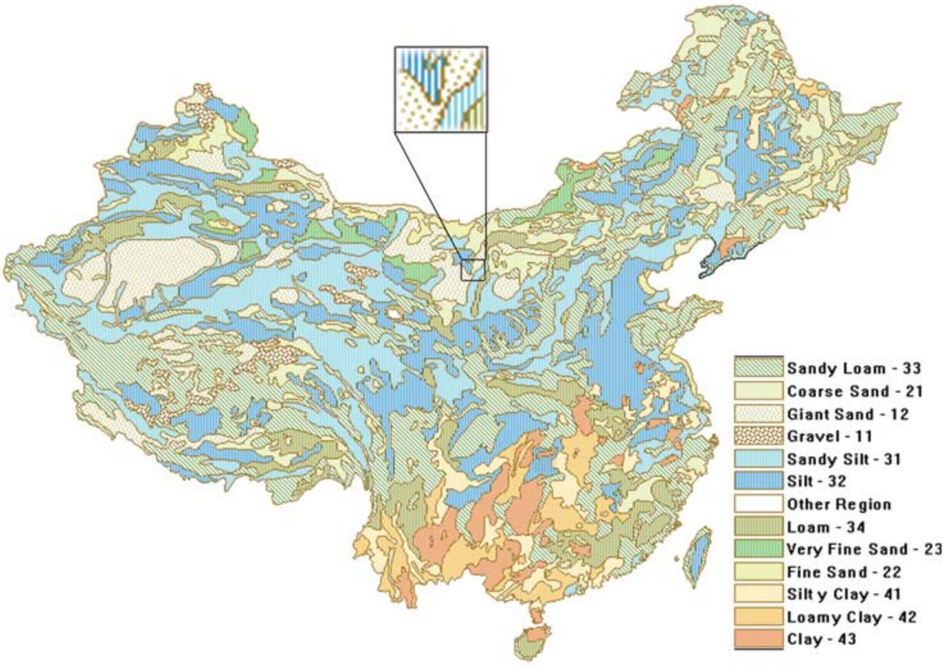

Figure 2. Chinese soil texture distributions and a sample grid with fractional coverage of mixed soil textures. The soil texture reflects the soil grain-size distributions. The legends and size ranges are given in Tables 1 and 2.

ments [*Alfaro et al.*, 1997]. Application of this scheme to the Asian deserts has not been extensively examined. The parameters which are applicable to the Asian dust aerosol emission are discussed in section 2.3.

2.3. Input Parameters for Chinese Deserts

[16] The previous section shows that the most critical parameters controlling the vertical soil dust flux are the surface wind speed, surface roughness length, soil texture, and moisture content. This vertical flux together with its size distribution determines the soil dust source function to be used in the model. There is very limited information with respect to a global soil grain-size distribution. In this simulation, a detailed Chinese soil texture map [*Hseung*, 1984] was used to derive the soil grain-size distribution and composition. Outside China, the global 1° × 1° data set of soil type and particle size [*Webb et al.*, 1991; *Zobler*, 1986] is used.

2.3.1. Modern Chinese Desert Distribution and Soil Texture/Grain Size

[17] Accurate simulation of soil dust aerosol generation and transport requires exact specification of the desert surfaces. The 1 × 1 km^2 surface land use data from EROS Data Center Distributed Active Archive Center (EDC DAAC), and they have been widely used in previous soil dust simulations. The desert group in this data set includes desert and semidesert. However, after a careful comparison of this data set with the current Chinese Desertification Map (CDM) [*CAS*, 1998], it was apparent that some deserts in northeast China (e.g., deserts 9 and 10 in Figure 1) and other regions have been omitted from the EROS data set. The CDM is based on the data collected during the 1980s and 1990s and reflects the most up to date desert distributions in China. Consequently, the soil dust uplift regions within China in this simulation were determined from the CDM data set. The impact of differing desert distributions on the surface soil dust concentrations in China and downwind regions will be discussed in the section 3.

[18] Another parameter that influences the dust uplifting flux is the soil grain-size distribution, which is governed by soil texture. The characteristics of soil texture in a region are mainly determined by the type of soil parent material and its mineral composition, and may also be impacted by cultivation and fertilization in farmland. Generally, soil texture evolves from a complex combination of natural processes. Figure 2 illustrates the soil texture distributions for 12 categories [*Hseung*, 1984] based on a Chinese survey representative of the 1950s to the 1970s. For each category, there is a size fraction associated with each of three modes with diameter ranges: (1) 1–0.05, (2) 0.05–0.01, and (3) <0.001 mm. Table 1 summarizes the approximate percent-

Table 1. Classification of Chinese Soil Texture and Size Fraction [*Hseung*, 1984]

Texture			Size Fraction, % (*d*, mm)		
Group	Map Legend	Category	Sand (1–0.05)	Silt (0.05–0.01)	Clay (<0.001)
Gravel	1_1	gravel			
	1_2	giant sand			
Sand	2_1	coarse sand	>70		<30
	2_2	fine sand	≥60–70		
	2_3	very fine sand	≥50–<60		
Loam	3_1	sandy silt	≥20	≥40	
	3_2	silt	<20		
	3_3	sandy loam	≥20	<40	
	3_4	loam	<20		
Clay	4_1	silty clay			≥30–<35
	4_2	loamy clay			≥35–≤40
	4_3	clay			>40

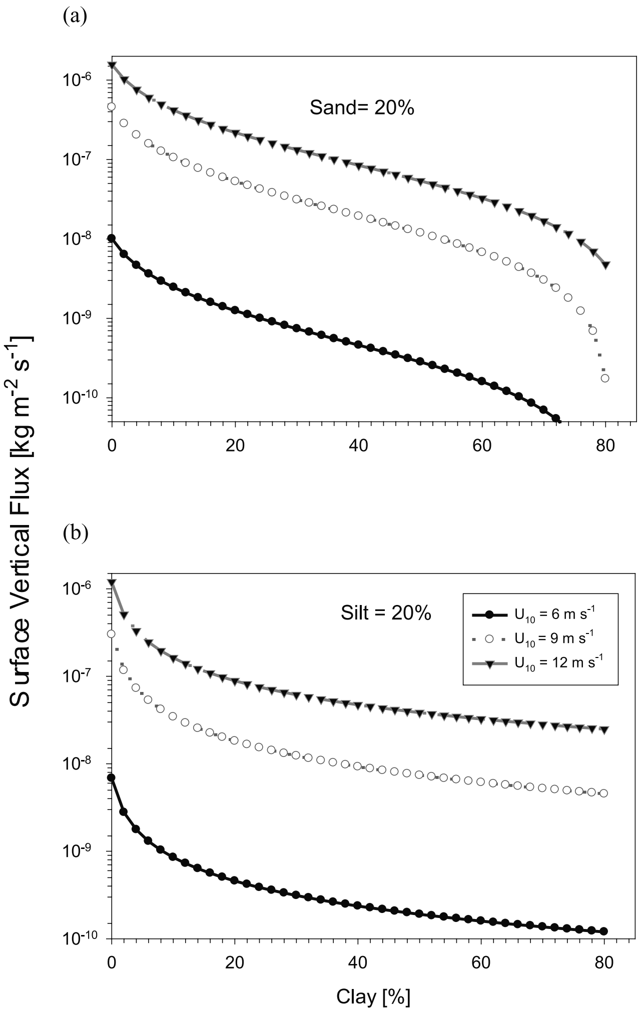

Figure 3. Impact of clay content on the vertical fluxes of soil dust aerosols. For any grid, the sum of clay, silt, and sand is 100%.

age ranges of each mode for all 12 categories. In Figure 2, a sample model grid is placed on top of the texture graph. For each model grid, a percentage of each category is calculated for the model input. The dominant sand coverage in this texture data set corresponds well with the CDM data with the exception of some newly developed desertification areas. For these areas, a modification to the texture data by new sand fraction was applied to reflect the current sand distributions. This generates a unified desert distribution and texture data set for Chinese soil dust simulations. Figure 1 illustrates the CDM in the simulation domain where 10 Chinese deserts are marked. Soil dust vertical flux was calculated only from grids with a desert fraction >3%.

[19] It should be noted that the soil-size compositions for each category in each grid contain uncertainties (Table 1). When they are used in the soil dust flux calculations, these uncertainties propagate to the flux and transport. Figure 3 shows the impacts of clay percentage on the vertical flux with fixed sand and silt at various wind speeds. It is obvious that at fixed 20% silt (Figure 3), 10% increases in clay content, i.e., decreases in soil-size distribution, result in a decrease of vertical dust flux by as much as 1 order of magnitude. By sensitivity analysis from the model simulations and comparisons with source region dust observations, the most appropriate parameters for grain-size distributions were determined based on the data in Table 1. For each mode of a soil category, a lognormal distribution is assumed. Table 2 shows the mass mean diameter (MMD, μm), standard deviation (σ), and percentage used in our simulations. For other regions, only two modes were utilized in the model based on the global 1° × 1° data set [*Webb et al.*, 1991; *Zobler*, 1986] with one mode (sand) of MMD = 690 μm, σ = 1.6, and another mode (silt) of MMD = 210 μm and σ = 1.8. Percentages for each mode were given by *Zobler* [1986].

2.3.2. Soil Moisture Contents

[20] The soil moisture content is simulated in the model by the Canadian Land Surface Scheme (CLASS) for GCMs [*Verseghy*, 1991]. This scheme includes three soil layers, a snow layer where applicable, and a vegetative canopy treatment. The averaged volumetric liquid and frozen moisture contents are modeled for each soil layer as prognostic variables. The layer depths currently used are 0.10, 0.25, and 3.75 m.

[21] The soil moisture content in the first model layer (0.10 m) was used to drive the soil dust emission scheme. As moisture content depends on the liquid water flow rate at the top and bottom of each layer, the balance of the surface layer evaporation and precipitation will determine the top flow rate. Given that precipitation prediction is a weakness in atmospheric models, predicted surface soil moisture contents are subject to significant error. Remote sensing may provide some spatial coverage of the soil moisture, but the agreement between remotely sensed and gravimetric soil moisture estimates are still not acceptable [*Laymon et al.*, 2001].

[22] Figure 4 shows the three 10-day-averaged soil moisture content distributions in April 2001 from model simulations and from field measurements in China. Observed and predicted values agree to within a factor of 2, while the spatial distributions of arid and semiarid regions are reasonably well represented. However, because of limited observations within the deserts and the 10-day-averaged observations, it is difficult to judge the accuracy of the model prediction of soil moisture content over the region. This suggests that accurate remote sensing of the surface soil moisture is imperative in both forecasting and modeling of soil dust aerosols.

Table 2. Derived Size Distributions of 12 Chinese Soil Categories

Texture			Size Distribution, *d*, μm								
			Sand			Silt			Clay		
Group	Map Legend	Category	MMD	σ	%	MMD	σ	%	MMD	σ	%
Gravel	1_1	gravel	1000		90	100		10	10		0
	1_2	giant sand	690		60			30			10
Sand	2_1	coarse sand	520	1.6	60	100		30	5		10
	2_2	fine sand			50	100		35	5		15
	2_3	very fine sand			45	75	1.7	40	2.5		15
Loam	3_1	sandy silt	520	1.6	35	75		50	2.5	1.8	15
	3_2	silt	210	1.7	30						20
	3_3	sandy loam	210	1.7	30	50			2.5		20
	3_4	loam	125		20				1.0		30
Clay	4_1	silty clay	100	1.8	65	10	1.8	0	1		35
	4_2	loamy clay			60				0.5		40
	4_3	clay			50				0.5		50

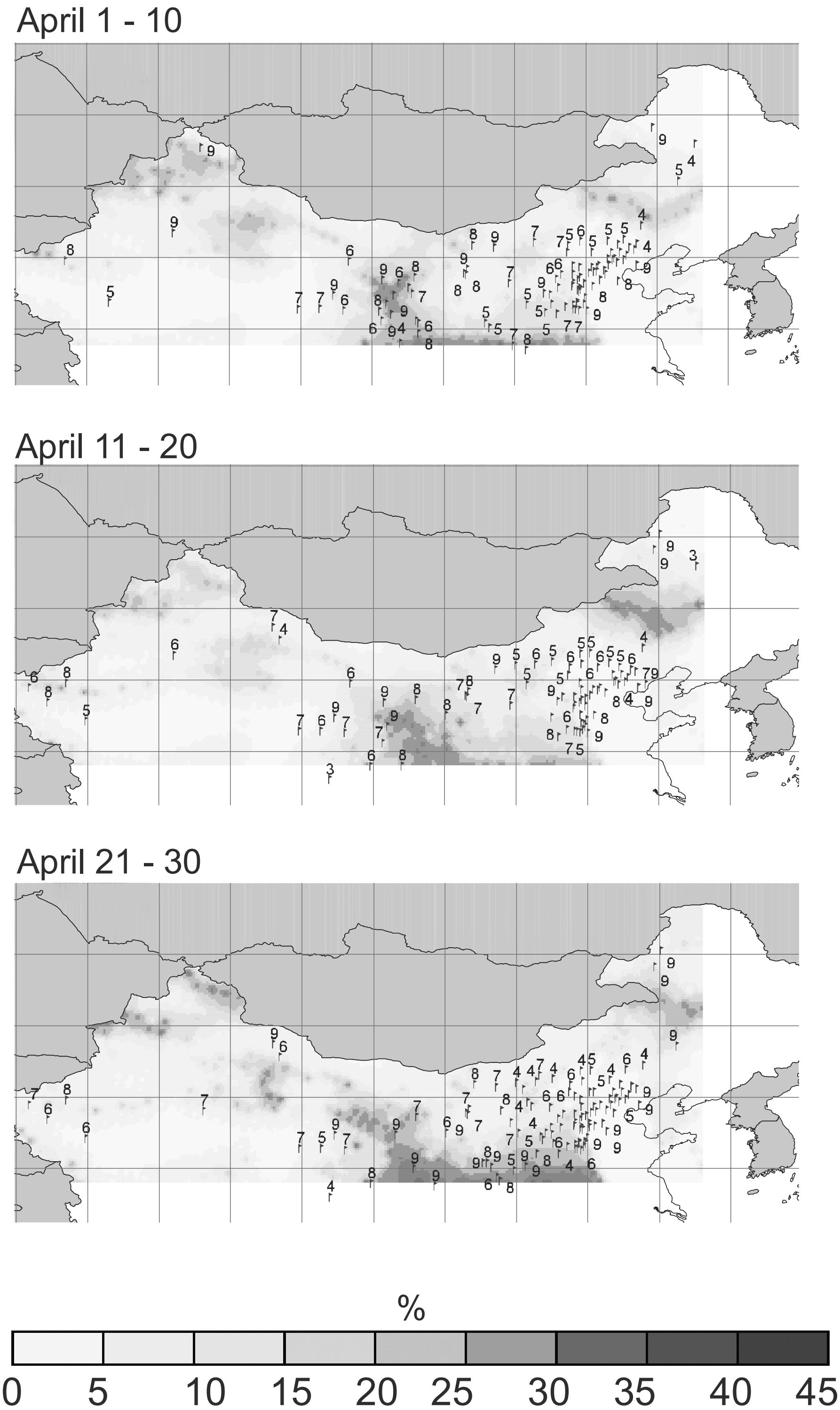

Figure 4. Model-predicted soil moisture contents in China and the comparison with the field measurements of three 10-day-averaged soil moisture in April. The numbers shown in the graphs are the field measurement data agreed by the model predictions within a factor of 2.

2.3.3. Land Use and Surface Roughness Length

[23] The 1 × 1 km^2 surface land use data have also been used in CAM for dry deposition calculations [*Zhang et al.*, 2001]. Fifteen land use categories (Table 3) are obtained from regrouping the 1 × 1 km^2 satellite data of the biosphere-atmosphere transfer scheme (BATS) [*Dickinson et al.*, 1986] to form the roughness density F of each category in a grid depending on the model resolution. To account for

Table 3. Land Use Categories (LUC) and Physical Height (h)

Category	Description	h, cm
1	evergreen-needleleaf trees	2000
2	evergreen broadleaf trees	4000
3	deciduous needleleaf trees	2000
4	deciduous broadleaf trees	2000
5	mixed broadleleaf and needleaf trees	3000
6	grass	20
7	crops, mixed farming	20
8	desert	0.2
9	tundra	0.2
10	shrubs and interrupted woodlands	100
11	wet land with plants	2
12	ice cap and glacier	0.01
13	inland water	0.001
14	ocean	0.001
15	urban	1000

the impact of nonerodible elements in a grid on the threshold friction calculation, a physical height (h) is assigned to each land use (roughness element) [*Pielke*, 1984]. The linear relation between roughness length Z_0 and h and the roughness density F is defined by *Marticorena et al.* [1997] as

$$Z_0/h = \begin{cases} 0.479F0.001 & F < 0.11 \\ 0.005 & F > 0 \end{cases}. \tag{11}$$

These relationships allow calculation of the roughness length for each roughness element from the roughness density and the height of the roughness elements.

[24] The effective roughness length Z_m is introduced into soil dust module to give the correct spatial average wind friction velocity over a grid box and is usually used in the parameterization of heterogeneous surface and terrain in large-scale models. *Taylor* [1987] suggested that one practical definition of an effective roughness length Z_m from a spatial average of the logarithm of the local micrometeorological roughness length over a model grid square is given by

$$\ln Z_m = \overline{\ln Z_0},$$

where $\overline{\ln Z_0}$ is a grid-square average over the 12 land use categories. Figure 5 clearly shows the impacts of roughness lengths (z_{0S} and Z_0) on the total vertical dust fluxes. Increases in z_{0S} will increase the vertical flux, while increases in Z_0 will decrease the vertical flux. The influence of Z_0 is more effective at lower wind speed (6 m s^{-1}), indicating that at this range of wind speeds the threshold of friction velocity and vertical flux are more sensitive to the value of Z_0 used in the model. This may not have a great impact on the dust storm flux, but it certainly will affect the local blowing dust distributions.

2.3.4. Size Distribution of Vertical Dust Flux

[25] In order to simulate dust loading and transport, together with optical properties, the size distribution of the vertical dust flux must be reasonably estimated [*Balkanski et al.*, 1996]. Measurements of the size distribution of soil dust in Chinese source regions within and on the edge of deserts have been analyzed in the companion paper [*Zhang et al.*, 2003] and are used here to elucidate a typical dust size distribution over Chinese deserts. Table 4 shows

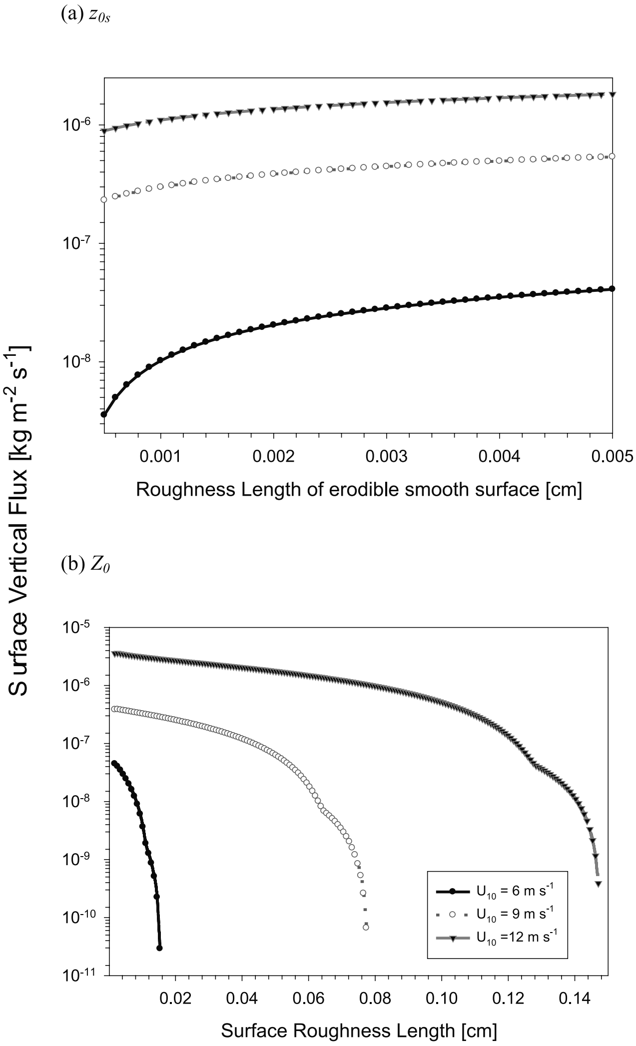

Figure 5. Impact of surface roughness length on the vertical fluxes of soil dust aerosols.

observations during 1994–2001 from selected Chinese deserts [*Zhang et al.*, 2003]. The impactor for measuring the dust-size distribution only gave fractions for particles <0.25 μm and >16 μm due to the size cutoff. Between 0.25

Table 4. Average Size Distributions for Ground-Based Mineral Aerosol During Local Dust-Storm Events at Five Desert Sites in Spring of 1994 and 2001

	Size Distribution (d, μm) (Mean of Al and Si Data)				
		0.25 to 16 (Lognormal Distribution)			
	<0.25 %	MMD	σ	%	>16 %
Eight Zhenbeitai samples, 2001 (Mu Su Desert)	0.52	3.7	1.5	72	28
Six Dunhuang samples, 2001 (Kumutage Desert)	0.37	5.2	1.5	74	26
Six Qira, Aksu, Jartai samples, 1994 (Taklimakan and Ulan Buh Desert)	4.7	7.3	1.6	69	25
Twenty samples, 1994 and 2001 (Average of Chinese deserts)	1.7	4.5	1.5	69	30

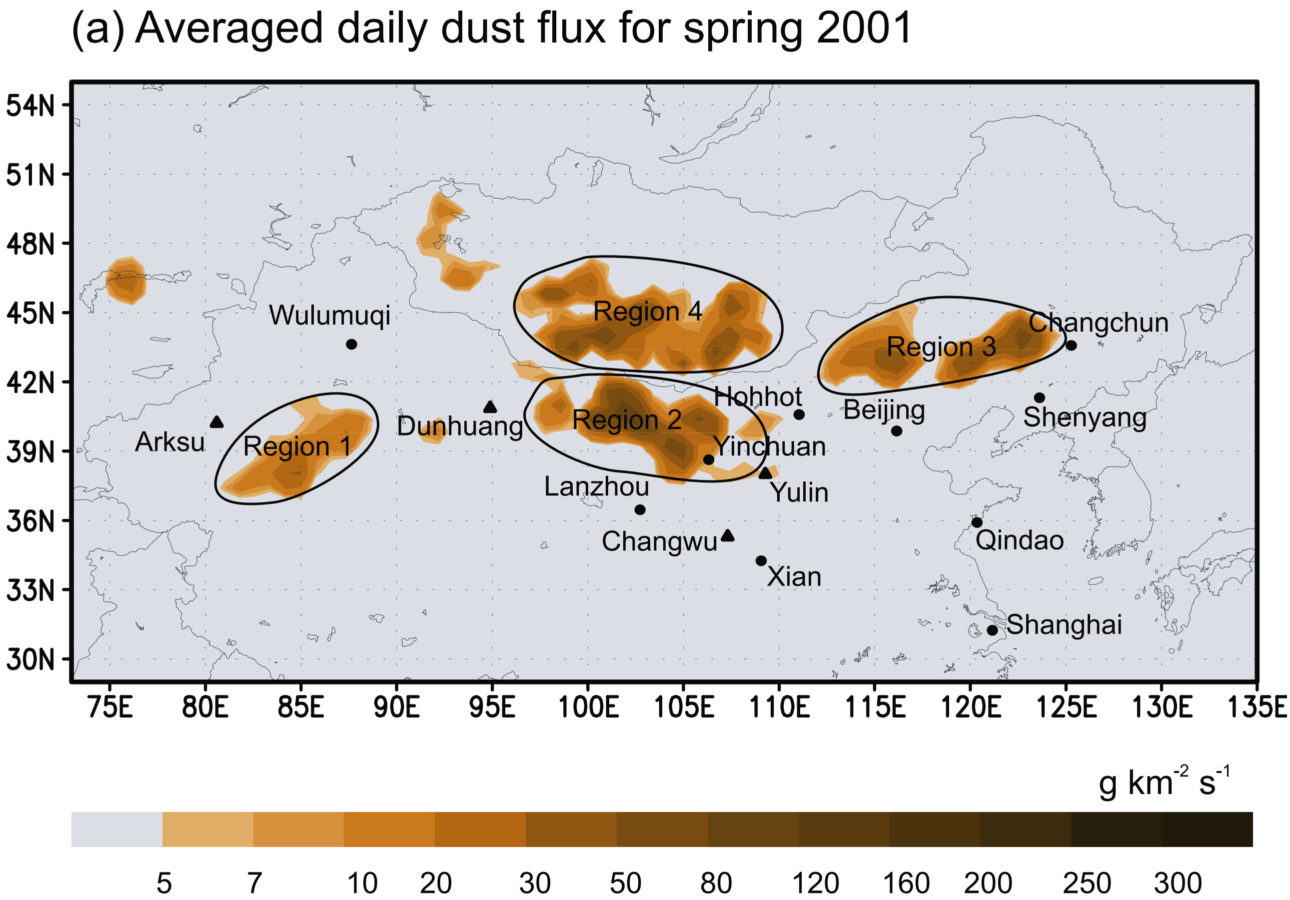

Figure 6. (a) Distributions of the averages of the daily soil dust vertical flux for spring 2001. The solid circles indicate the comparison stations where PM_{10} concentrations derived the air quality index were done with simulations in Figure 8. The solid triangles indicate the stations where direct measurements of total PM were made and compared with model results in Figure 10. (b) Distributions of the averages of the daily soil dust vertical flux for each dust storm.

and 16 μm, observations were reasonably approximated by a lognormal fit (Table 4). The averaged size distributions over China were used in this simulation for the size distribution of the vertical fluxes.

3. Simulation Results and Discussions

[26] Observations of soil dust from the Chinese Dust Storm Research (ChinaDSR) observational network stations are presented in a companion paper [*Zhang et al.*, 2003]. The objective of this paper is to compare model results with observations, investigate the transport and distribution patterns of soil dust during the spring 2001 ACE-ASIA period, and examine the model performance with respect to input parameters. The model was run on a polar stereographic projection with a horizontal resolution of 100×100 km^2 and 22 vertical levels on a Gal-Chen terrain following coordinate from ground to 30 km. The integration time step was 20 min. Twelve diameter classes from 0.01 to 41 μm were used to represent the size distribution of soil dust. Dust fluxes and concentrations were calculated for each size bin. The model domain covered East Asia, North Pacific, and west North America (Figure 1). Five regions A, B, C, D, and E were chosen in the domain to represent the source region in China and receptor regions in China, East Asia, mid-Pacific, and western North America, respectively. The most southern edge of the Chinese receptor region was set at 28°N, beyond which no historical records of soil dust deposition were found [*Zhang*, 1984]. This region was further divided into B_1 and B_2, representing the Loess Plateau and other parts. The dots in Figure 1 illustrate the center of model grid, while the deserts outside China are shown by green contours.

3.1. Spatial Distributions and Time Series of Dust Aerosols During ACE-Asia

[27] Model simulations of four mixed aerosols of soil dust, sulfate, sea salt, and black carbon were conducted for 4 months from 1 February to 31 May 2001. The last 3 months of results were used in this study to compare with the ground observations of soil dust aerosols across China and to investigate trans-Pacific transport. During this period, four major dust storm episodes were observed [*Zhang et al.*, 2003] around the following days: 2–6 March (dust storm 1 (DS1)), 21–26 March (DS2), 4–14 April (DS3), and 29 April to –4 May (DS4). The spatial and temporal distributions of soil dust simulated over these major dust storm episodes are presented with observations for comparison. Figure 6a shows the average of the daily

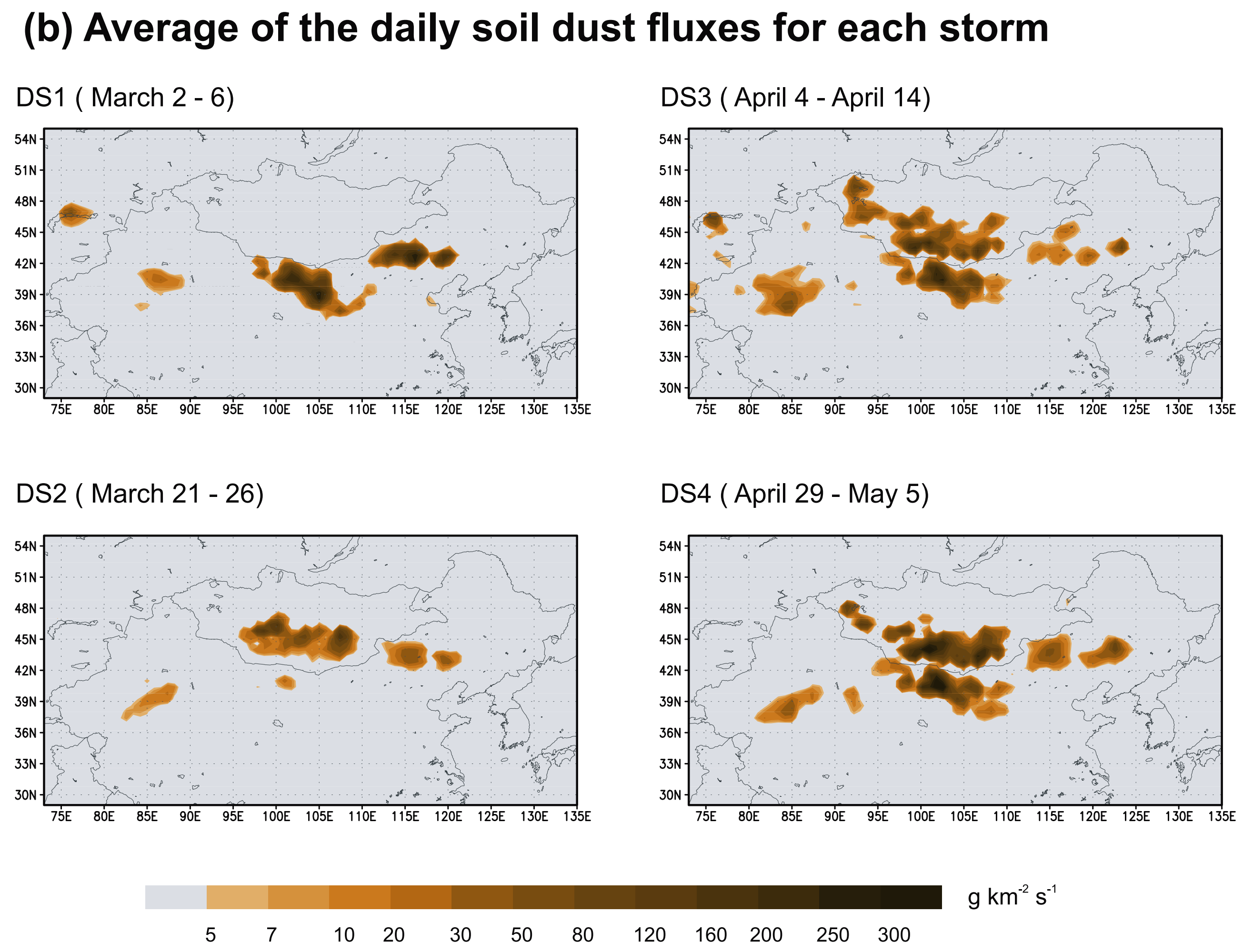

Figure 6. (continued)

vertical soil dust flux for spring 2001. The dust flux distributions illustrate the source regions during ACE-Asia. Four major source regions in East Asia were identified from Figure 6a: (1) Taklimakan desert in Xinjiang Province, (2) desert groups (deserts 4, 5, 6, 7, and 8 in Figure 1) in west and middle Inner Mongolia, (3) Onqin Daga and Horqin deserts in northeast Inner Mongolia, and (4) the Gobi desert in Mongolia. Figure 6b shows the averages of the daily vertical dust fluxes over each dust storm episode. From 1 March to 31 May 2001, the total dust mass emitted in regions A + B was 252.8 Mt, among which 22, 12, 66, and 51 Mt were attributed to DS1 (5 days), DS2 (6 days), DS3 (11 days), and DS4 (7 days), respectively. The four dust storms accounted for about 60% of the total mass emitted.

[28] The first major dust storm (DS1) of spring 2001 started on 2 March and was associated with a cold front emanating from northwest of Xinjiang Province that brought strong winds to the Taklimakan desert and uplifted dust clouds. One day later, on 3 March, this air mass passed the west and middle Inner Mongolian deserts that include Badain Juran, Tengger, Ulan Buh, Hobq, and Mu Us, resulting in visibilities of <1 km in that area. On 5 March, this system moved to the northeast Inner Mongolia and caused dust emissions from Onqin Daga and Horqin deserts, resulting in heavy dust clouds seen by Total Ozone Mapping Spectrometer aerosol index (TOMS AI) over northeast China on 6 March.

[29] DS2 started around 21 March and lasted 6 days. This dust storm was associated with a cold front that influenced Taklimakan, Ulan Buh, Hobq, and Mu Us deserts. Compared with DS1, the daily-averaged flux from our model simulation (Figure 6) indicates that this storm originated mostly from the Gobi desert in Mongolia rather than in the Chinese deserts. During DS1, the cold front passed across the Gobi desert but did not cause any significant dust emission. Model results showed that snow cover and soil moisture content changes from 2 March to 21 March played a significant role in entraining dust from Mongolia during DS2.

[30] The largest dust storm (DS3) during ACE-Asia originated from Xinjiang when a vigorous cold front on 4 April generated strong northeast winds of up to 20 m s^{-1}. Over the edge of Taklimakan and Tsaidam Basin deserts, large dust clouds were observed and the visibility was reduced to <1 km over the Tsaidam Basin desert. On 5 April, this system moved eastward to the west Inner Mongolia and dispersed. A second front on 6 April uplifted heavy dust clouds over Taklimakan desert in Xinjiang and all deserts in Inner Mongolia of China as

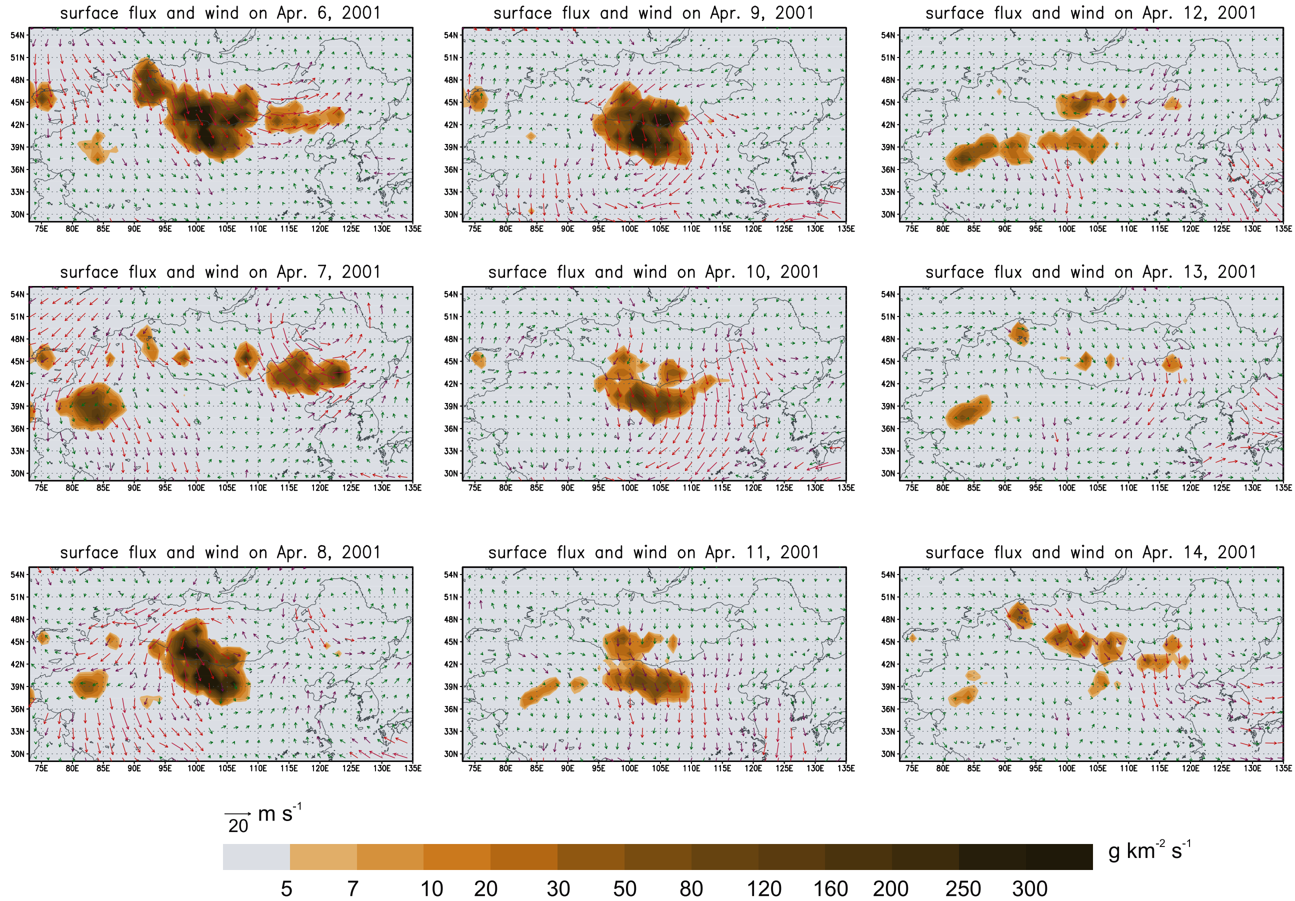

Figure 7. Daily-averaged surface soil dust fluxes and 10-m wind vectors for DS3 from 6 to 14 April 2001. The color of the arrows defines the strength of wind speeds: <5 m s^{-1} (green), 5–10 m s^{-1} (purple), 10–20 m s^{-1} (orange), >20 m s^{-1} (red).

well as over Gobi desert in Mongolia. This is clearly shown in the daily-averaged dust flux from the simulation for this episode (Figure 7). On 7 April, this storm moved eastward to the northeast part of China and produced a widespread region of poor visibility in northern China. The worst affected region was in northeast China where visibility dropped to <1 km. According to the model simulations, the major contribution of soil dust to this region was from the Onqin Daga and Horqin deserts in Inner Mongolia (Figure 7). These two deserts were omitted from the EROS satellite-based land use data set. Both model-predicted fluxes and surface concentrations confirmed the contributions from these two deserts. On 8 April, this air mass moved out of northeast China and the visibility in northern China improved substantially. In the meantime, another cold front developed over Taklimakan, Tengger, and Gobi deserts and generated a third wave of dust clouds in these regions. This system shifted from northwest to northeast China and Mongolia and the dust clouds persisted over the Taklimakan and the west Inner Mongolia deserts until 14 April.

[31] The last major dust storm in spring 2001 began at the Chinese Taklimakan and Mongolian Gobi deserts on 29 April. One day later, an area of visibility <1 km was formed over the Onqin Daga desert and further developed to cover most of Beijing on 1 May.

[32] These four major dust storms and other minor ones were recorded daily in the ground air quality index (AQI) reports in major Chinese cities by SEPA (China Environmental Protection Network, State Environmental Protection Administration of China, Beijing, 2002, available at http://www.zhb.gov.cn/index4.htm). The equivalent PM_{10} (particulate matter <10 μm) concentrations (EPMs) for 1 March to 31 May 2001 were deduced from the AQI data. Although it includes all particulate matter sources, this EPM is a good indication of relative dust concentrations across China, especially for dust episodes. Figure 8 shows the comparison of time series of soil dust concentrations from the model simulation and EPMs from AQI data among six stations (Figure 6a) from West to East China. As this is only a relative comparison of dust concentrations, the simulated and observed concentrations were plotted on two separate vertical axes with slightly different scale to match the peak concentrations. It is obvious that the CDM + EROS data set generates more reasonable dust peak time series than the EROS satellite data, indicating the importance of accurate desert distributions in the soil dust simulations. However, sometimes, the CDM + EROS data also overestimated the dust peak in the model either due to the overestimate of the desert coverage or underestimate of the soil moisture.

[33] Model simulations utilizing the CDM data (which includes deserts in northeast China not included in the

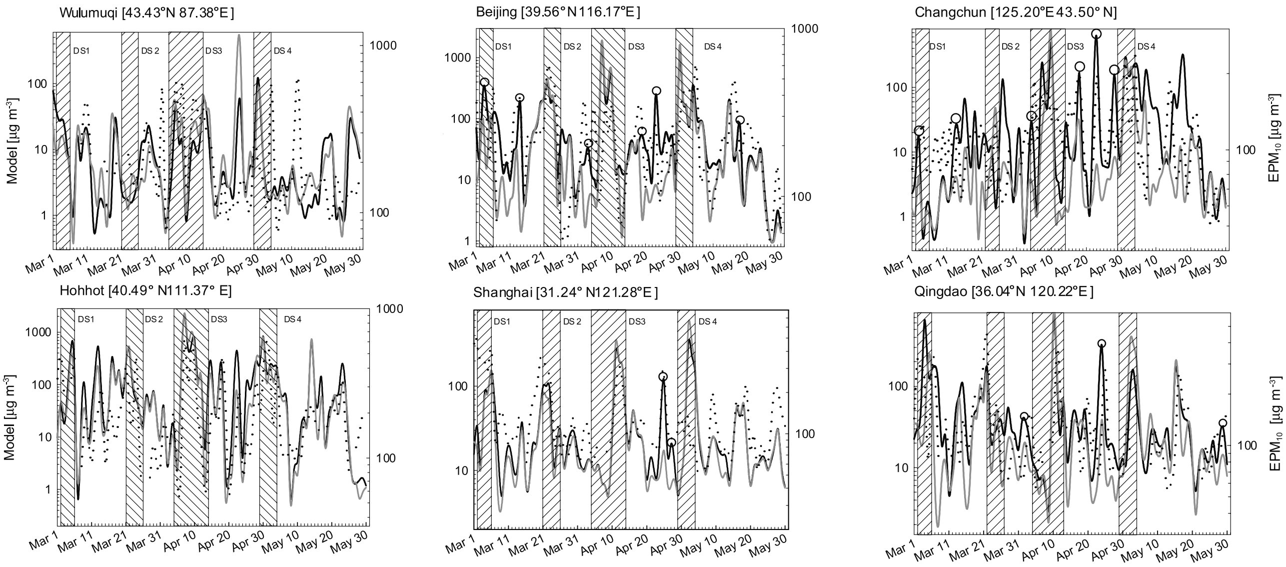

Figure 8. Comparisons of modeled time series of dust concentrations over China with air quality index derived PM_{10} concentrations (dots) for six cities. The two curves shown represent simulations using input from the EROS satellite data (gray line) and CDM + EROS data (black line), respectively. The open circles on each plot identify the improvements of the CDM + EROS data set to correctly predict the dust peaks, especially for cities in northeast China. Local time is used for the plots.

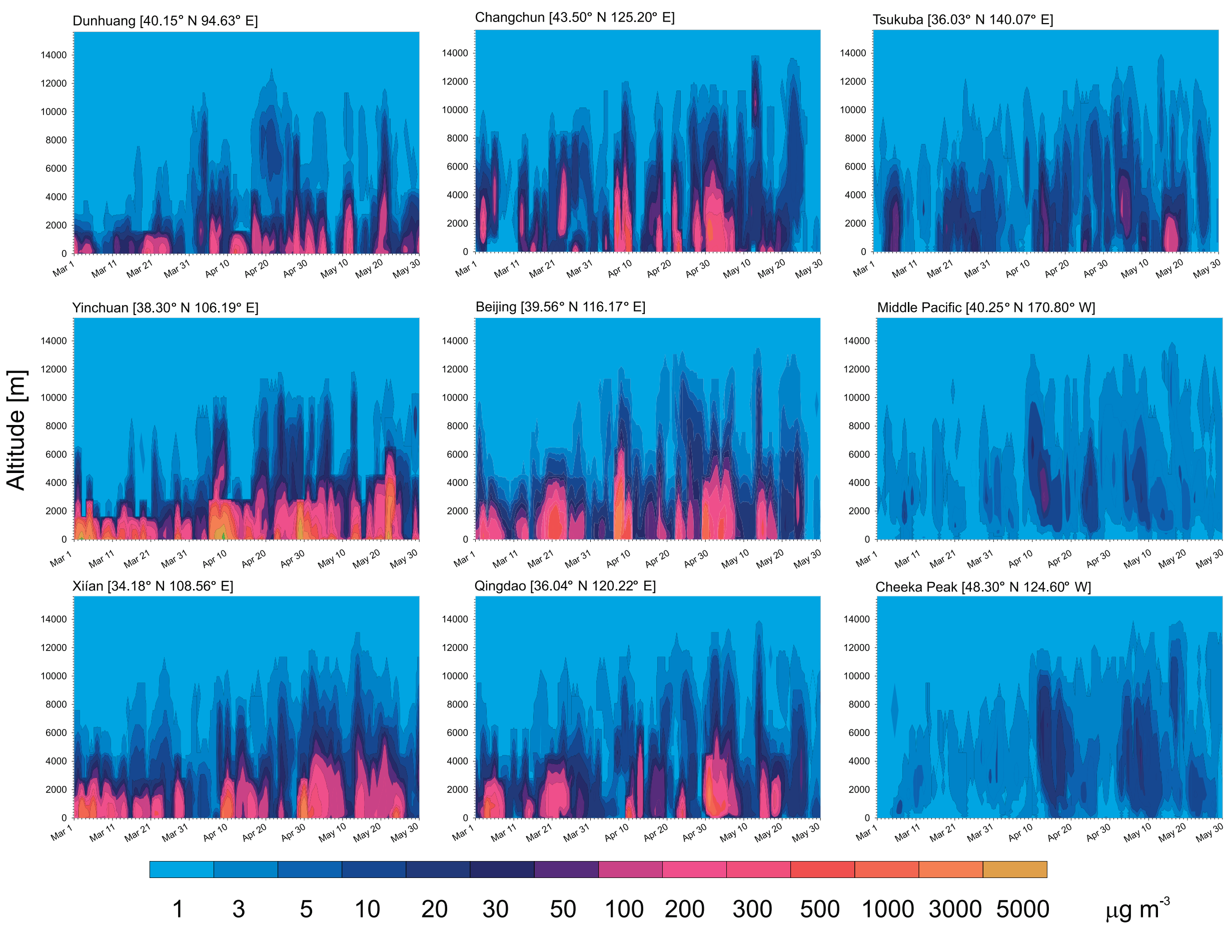

Figure 9. Time vertical profiles of soil dust concentrations for selected locations for spring 2001 ACE-Asia. Local time is used for the plots.

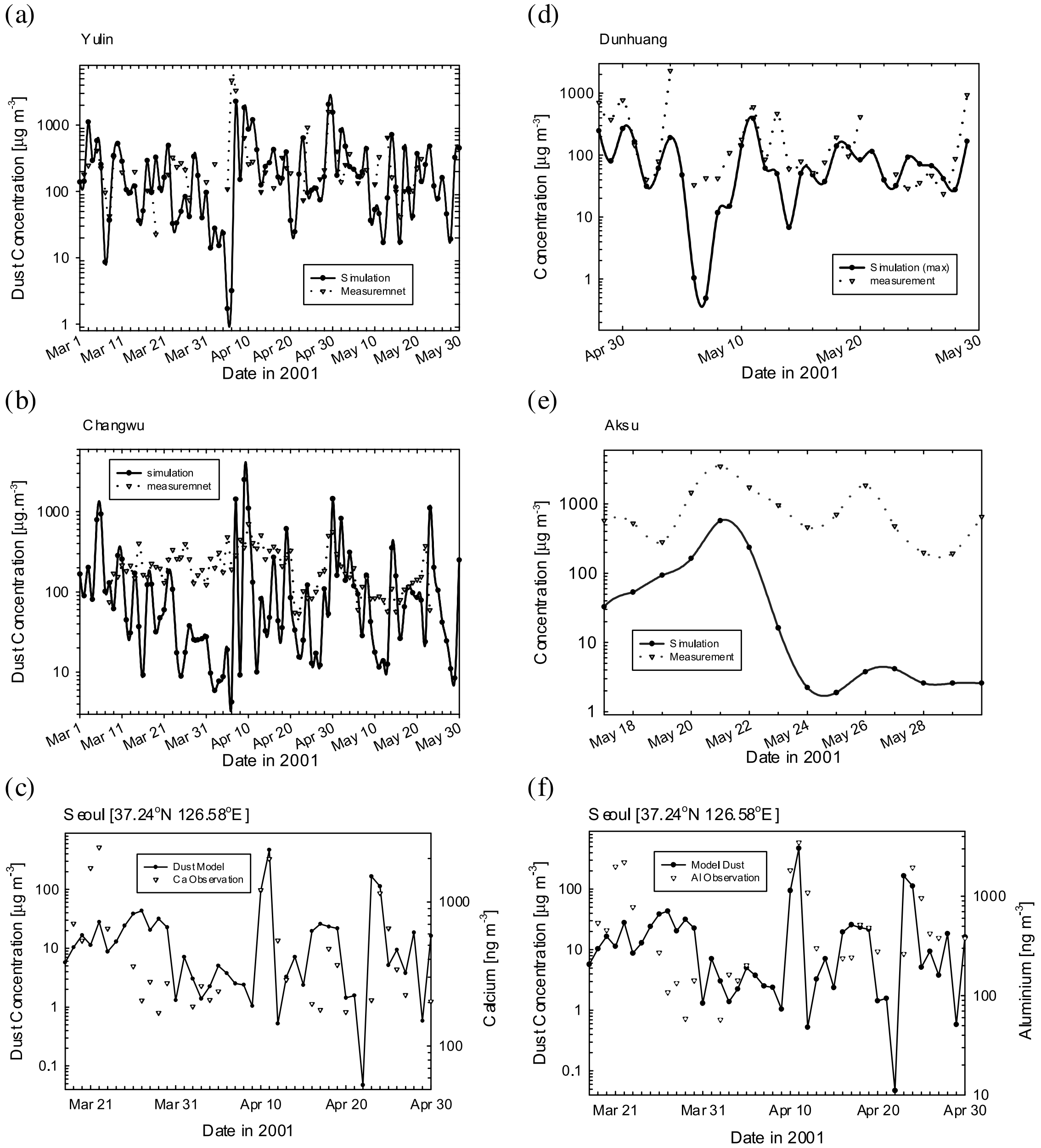

Figure 10. Comparisons of model-predicted dust concentrations with surface measurements of dust concentrations in China and elemental Ca and Al in aerosols at Seoul, Korea, during ACE-Asia. Local time is used.

EROS satellite data) performed best for the DS3 episode on 7 April and serves to illustrate the importance of including these regions in dust simulations. Both surface measurements and TOMS AI confirmed the heavy dust clouds over these regions. According to the surface fluxes (Figure 7), Onqin Daga and Horqin deserts were the major contributors of soil dust emission to this dust storm episode. Simulated vertical time series for selected locations in China and across the Pacific Ocean during spring 2001 are shown in Figure 9. These contours illustrate the vertical distributions of soil dust over a site and demonstrate the layer structures of soil dust transport. Peak dust concentrations generally occurred below 1000 m for sites close to source regions (e.g., Dunhuang and Yinchuan). For downwind locations in China (Xian, Beijing, Qingdao, and Changchun), the peak altitudes increased to a range from 1000 to 3000 m. The peak altitudes continued to increase downwind of China, reaching 2000–4000 m in Tsukuba, 4000–5000 m in the middle Pacific, and 5000–7000 m at Cheeka Peak on the west North American coast (Figure 1). As the dust moved across the Pacific, concentrations were reduced considerably by dry and wet deposition. It may also be noted that depending on the strength and location of the dust source, the heights at which dust may pass over a downstream location vary substantially from one episode to another. The peak altitudes are also governed by vertical mixing processes such as convection and turbulent diffusion of soil dust. A comparison of the

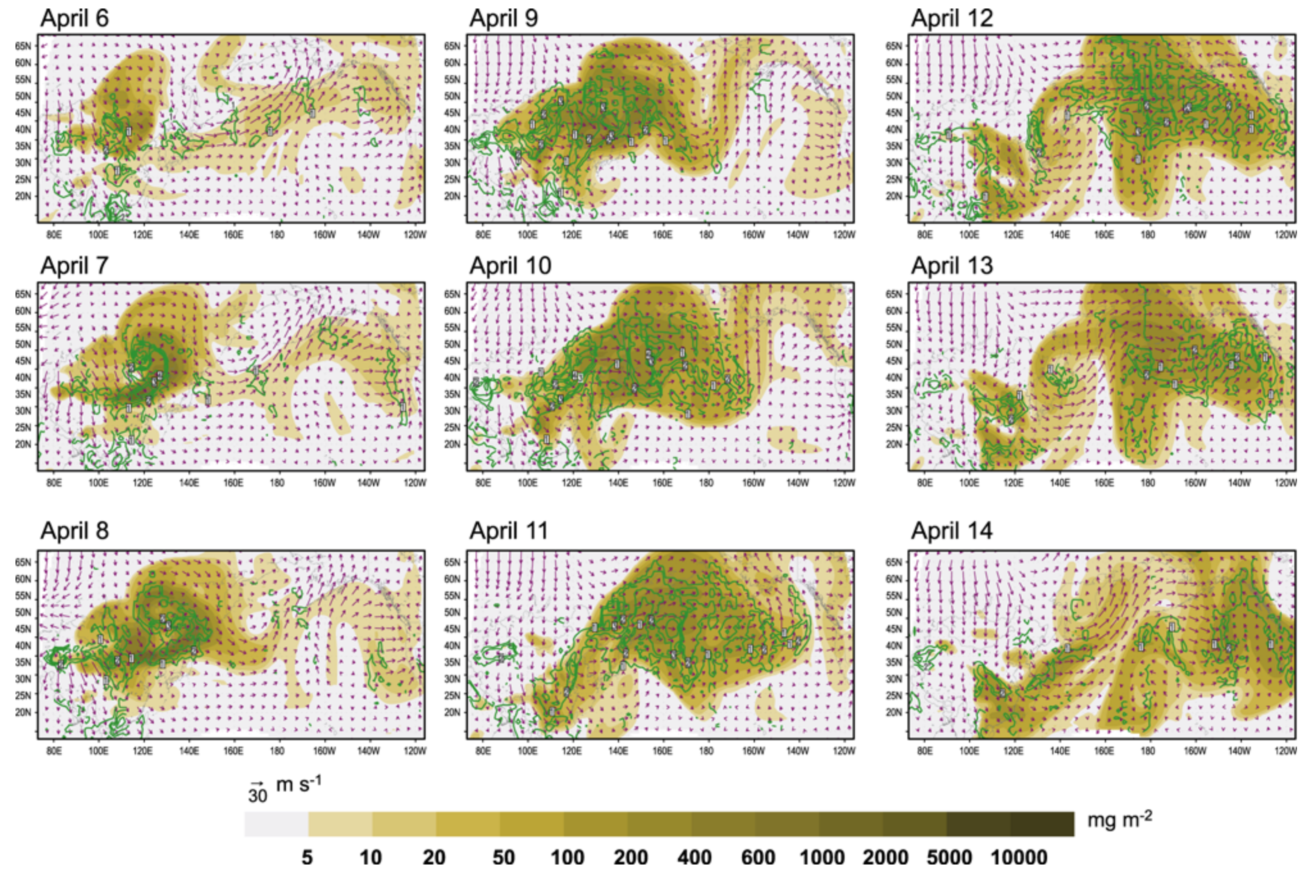

Figure 11. The daily dust column loading above 700 hPa and the TOMS AI from 6 to 14 April 2001 during DS3. The green contour lines are for TOMS AI, whose values are indicated by the numbers. Universal time (UT) is used for the plots.

vertical time series for Cheeka Peak observation is given in section 3.3 (Figure 14).

3.2. Comparison With Surface Observations

[34] Direct comparison of model predictions and surface measurements of soil dust concentration enables verification of absolute values of dust concentration simulated in both source and receptor regions. Figure 10 shows the time series from both observation and model predictions for Yulin, Dunhuang, Arksu, and Changwu in China and Seoul in Korea. It is evident that the model captures the prominent peaks in dust at these stations. However, for Yulin (Figure 10a) and Dunhuang (Figure 10d), which are located directly downwind of major deserts, the agreement between model prediction and observation is better than Changwu (Figure 10b) and Arksu (Figure 10e). This difference may be attributed to four main factors. First, sampling frequencies at Yulin and Changwu are different [*Zhang et al.*, 2003]. Yulin samples only northerly winds while Changwu samples all wind sectors 2 hours each in the morning and the afternoon. This noncontinuous measurement makes the comparisons rather difficult for an episodic event such as a dust storm. Second, it is highly probable that the measured and modeled peaks are not synchronized due to the difference in the observed and modeled meteorology. In order to match observations, the model needs to be accurate in terms of meteorology and transport to a resolution of the order of an hour. This is difficult to achieve. A daily-averaged observation is more appropriate to compare with model predictions. Third, the background PM contributions surrounding the monitoring stations were not properly modeled. This is revealed in the good comparisons during dust storm periods when the background PM was overwhelmed by the dust aerosols. Last, the observed and modeled meteorology may not match very well. This influences both dust emission and transport. The impact of soil moisture on the threshold friction velocity has been discussed in section 2.3.2. A comparison of the surface wind speeds for some selected grids with closest weather monitoring stations during dust storm episodes for the ACE-Asia period revealed that the model-simulated peak wind speeds generally correlate with the observed peak wind speeds, indicating that the model reasonably captured the high wind speed occurrences for the dust uplifting. However, the absolute values did not match very well. This is possibly due to the fact that the grid wind speed is averaged over the 100 $\times$ 100 km^2 grid square and the weather station wind speed is only indicative of limited area. For some stations, an apparent underestimate of the wind speeds may have contributed to an underestimate of soil dust concentrations in the model (e.g., Arksu in Figure 10e). The comparison of the surface dust concentrations in Seoul, Korea, with the surface Ca and Al measurements (Figures 10c and 10f) indicates that the dust arrival time at

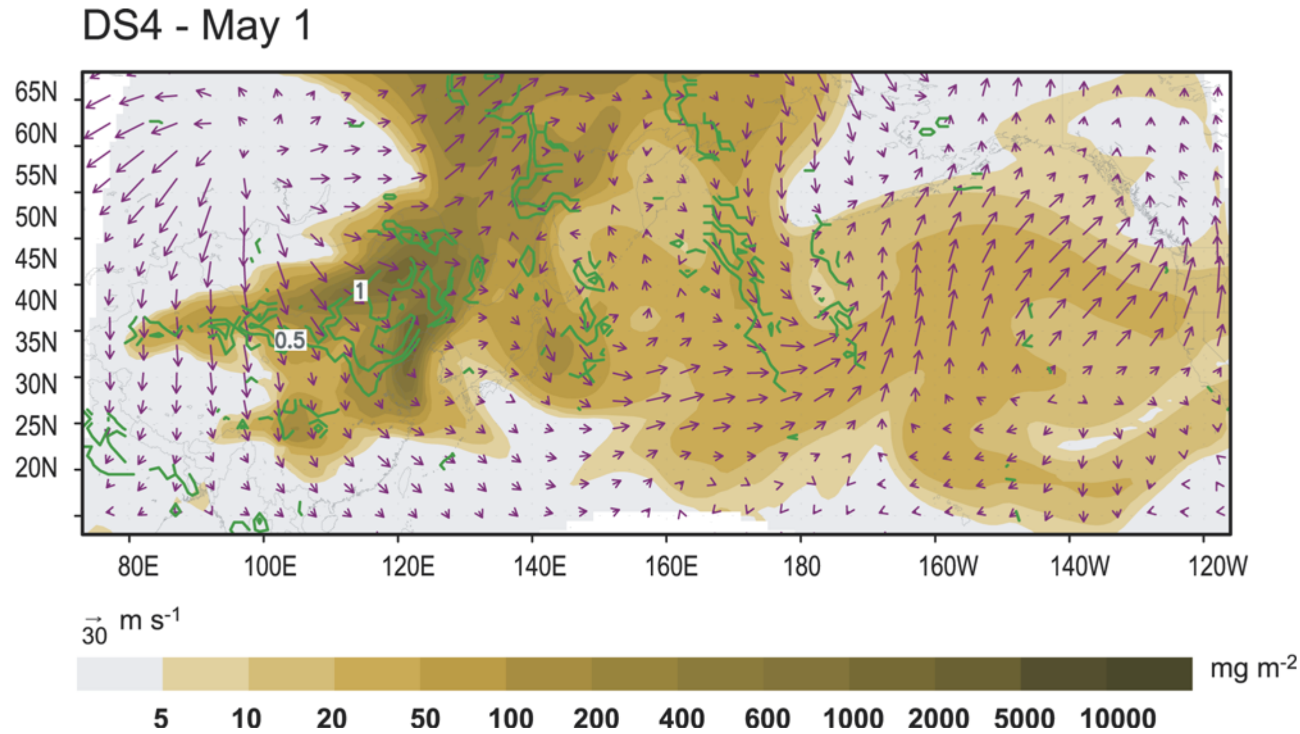

Figure 12. The dust column loading above 700 hPa and the TOMS AI on 1 May during DS4. The green contour lines are for TOMS AI whose values are indicated by the numbers. A deep trough that formed west of Japan promoted significant meridional flow, reduced the zonal airflow, and weakened the trans-Pacific transport. UT is used for the plots.

Seoul was reasonably simulated with the matching peaks of modeled dust and observed Ca and Al.

3.3. Trans-Pacific Transport

[35] Comparison of the TOMS AI with the simulated soil dust column loading distributions was performed to investigate the long-range transport of soil dust aerosols over the Pacific Ocean to North America. As TOMS has a limitation of detecting aerosols below 2 km above the surface [*Herman et al.*, 1997], dust aerosol concentrations above 700 hPa were used to compute the column loadings. A daily-averaged dust loading was extracted to compare with the TOMS AI. The goal of this comparison was to verify the dust column loadings and transport patterns over long distances from the source regions. By a careful analysis of TOMS AI values for the period of ACE-Asia, it was evident that DS3 was the most significant long-range transport event during the period. Figure 11 compares the daily spatial distributions of dust loading above 700 hPa from model simulations for the whole period of DS3 and the corresponding TOMS AI. On the same plots, the 500 hPa wind velocity fields are also shown to illustrate the synoptic transport patterns. A very good agreement between the spatial and temporal distributions of model-predicted dust loading and the TOMS AI was achieved.

[36] From surface flux plots for the same dust storm in Figure 7, it is apparent that the heavy dust clouds that reached the west coast of North America on 13 April originated from southern Mongolia and north-central China on 6 April and passed over Onqin Daga and Horqin deserts in northeast China on 7 April. DS4 also originated largely from the same locations as DS3 (Figure 6b). but less long-range transport to the mid-Pacific and west coast of North America was observed from TOMS AI.

[37] The strength and frequency of the dust storms that are engaged in long-range trans-Pacific transport are governed by both the source region strengths and the circulation patterns over the North Pacific Ocean. High wind velocity in the lower troposphere is necessary to generate dust storms if the soil moisture is below a threshold value. For DS3, a cold front associated with a Mongolian cyclone moved across the desert regions in Mongolia and northern China toward the southeast. This feature was associated with a westerly trough at 500 hPa where baroclinicity was well developed, causing strong dynamic motions. A very similar synoptic condition over the dust source regions in Mongolia and northern China was observed for DS4. This event had even larger daily surface fluxes and dust concentrations over East Asia than those for DS3. However, the dust plumes caused by DS4 over the west coast of North America were observed to be smaller than those by DS3 from TOMS AI. For region A (Figure 1), and the daily-averaged fluxes for each grid during DS3 and DS4 were 0.0062 and 0.0078 kg km^{-2} s^{-1}, respectively. However, the daily-averaged dust column loadings in region E for each grid, after 5 days' delay from the each dust storm in region A, were 33.50 and 32.63 (μg m^{-3}) for DS3 and DS4, respectively.

[38] During DS3, the major trough over Japan and the west Pacific at 500 hPa was weaker than that associated

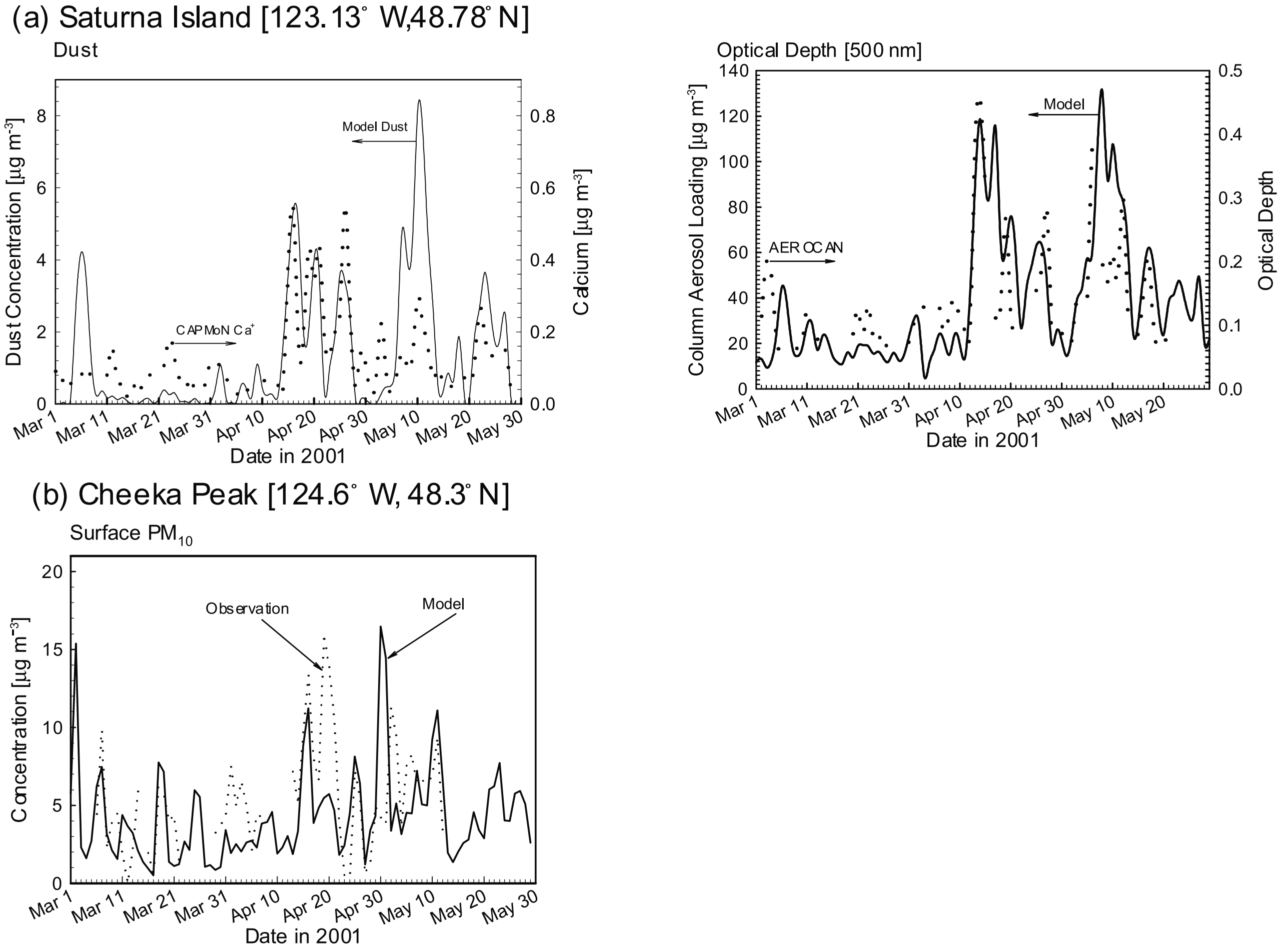

Figure 13. Comparison of model simulations with North American surface measurement data: (a) Saturna Island by CAPMoN and AEROCAN monitoring network, and (b) Cheeka Peak. Local time is used.

with DS4. This weaker trough favored a stronger zonal airflow for trans-Pacific transport. However, during DS4, a deep trough that formed west of Japan promoted significant meridional flow. This consequently reduced the zonal airflow and weakened the trans-Pacific transport of soil dust to North America. Figure 12 shows one of the typical circulation patterns for the DS4 transport and comparisons with TOM AI for that day. It is apparent that the East Asian major trough during DS4 was stronger and closer to the source regions than that observed during DS3. The stronger meridional flow carried the dust clouds farther north to Siberia (Figure 12) and weakened the strength of the dust clouds to be transported to the North America. TOMS observations seem to confirm this stronger DS4 trough with high aerosol index above 65°N over Siberia, which was not seen during DS3. It should be pointed out that the precipitation patterns along the path also play an important role in determining the residence time and strength of soil dust reaching western North America.

[39] The time series of predicted aerosol concentrations were compared with two monitoring stations in North America. Figure 13a shows the comparisons of the time series for soil dust (calcium) between model predictions and air filter measurements at Saturna Island (48.78°N, 123.13°W) by the Canadian Air and Precipitation Monitoring Network (CAPMoN). The soil dust peaks agreed reasonably well with the calcium peaks from the measurements, indicating that the arrival of dust at the surface on the west coast was satisfactorily predicted by the model. The optical depth measurements during spring by AEROCAN network station at Saturna was also compared (Figure 13a) with the column loading of the total aerosols simulated by our model. The peaks of the optical depth match reasonably well with the aerosol loading peaks by the model simulations, especially during the dust intrusion episodes. A similar level of agreement for west coast Sun photometer stations during the April 2001 dust event was obtained in a recent comparison with the NAAPS model and TOMS data [*Thulasiraman et al.*, 2002].

[40] At Cheeka Peak (48.3°N, 124.6°W), observed and modeled PM_{10} concentrations show the intrusion of dust particles to the ground station, especially for the DS3 episode (Figure 13b). In the vicinity of Cheeka Peak off the coast of Washington, the vertical profiles of the submicron aerosol scattering coefficients (tsg) were measured during spring 2001 using a Beechcraft Duchess aircraft

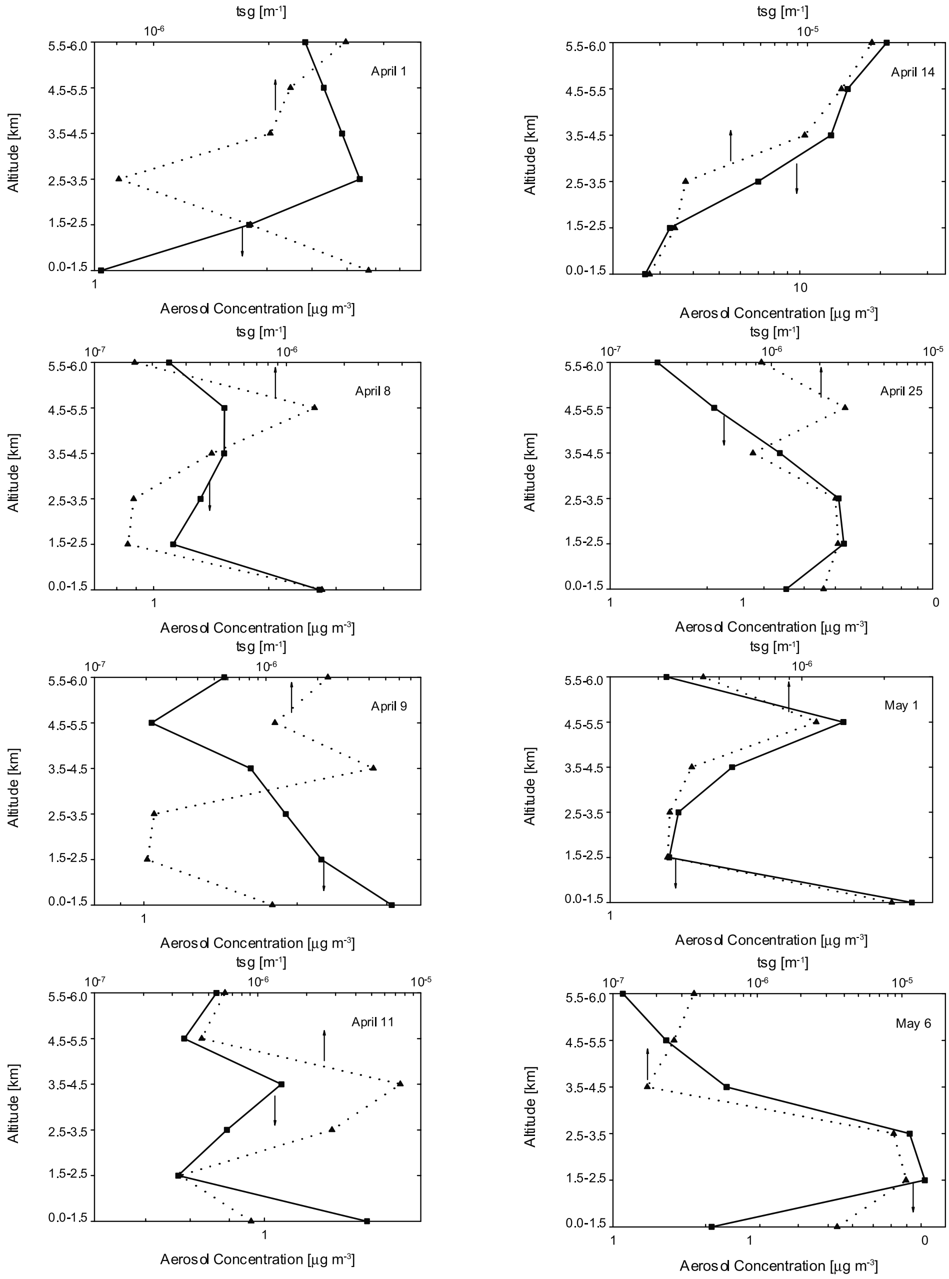

Figure 14. Comparison of the measured submicron aerosol scattering coefficient (tsg) and the model-predicted submicron aerosol concentration vertical profiles obtained near the Cheeka Peak Observatory on the coast of the Olympic Peninsula, Washington. Local time is used.

(H. Price et al., Vertical profiles of O_3, aerosols, CO, and NMHCs in the northeast Pacific during the Trace-P and ACE-Asia experiments, submitted to *Journal of Geophysical Research*, 2001) and compared with the submicron aerosol concentrations predicted by the model (Figure 14). The vertical profiles from 8 to 14 April clearly show the arrival of DS3 to the North American west coast peaked around an altitude of 4.5–5.5 km. On 14 April, both model and observation profiles exhibited a peak higher than 6 km, indicating a strong dust source aloft from the DS3 which originated in Asia around 8 April. The agreement between model predictions and aircraft measurements is reasonably good except for April 1 and lower level April 9 profiles. There was very reasonable agreement between model and observations for 1 and 6 May. The dust time vertical profile plot for Cheeka Peak during whole spring 2001 was also shown in Figure 9.

4. Conclusions

[41] Input parameters for the Chinese deserts that can be used for a detailed soil dust emission scheme have been investigated and verified against surface observations. The combined data sets for the desert distribution/texture, satel-

lite land use/roughness length, vertical flux size distribution, and observed soil moisture provide a coherent input parameter set for the size distributed soil dust emission scheme for Chinese deserts and show satisfactory results for simulations of the ACE-Asia period. The new Chinese Desertification Map (CDM) is required to accurately simulate the spatial and temporal distributions of dust storms in source regions and long-range transports of Asian dust to the North Pacific and North America.

[42] The model simulation of ACE-Asia soil dust storms for spring 2001 yields reasonable spatial and temporal distributions compared with the surface observations of the AQI across China and soil dust measurements from the Chinese Dust Storm Research observational network stations. Analysis of the dust storm distributions during ACE-Asia showed that there were four major desert groups that contributed most of the total dust fluxes in spring 2001. Soil dust from these deserts is mainly uplifted by synoptic weather patterns characterized by cyclones with intense cold fronts associated with troughs over the region from Mongolia to northwest China, north Xinjiang province, and northeast China.

[43] For regions downwind of the Chinese deserts, i.e., East Asia, mid-Pacific, and west North America, the simulated soil dust column dust loading correlates reasonably well with the TOMS AI spatially and temporally. It is found that the strength of the trans-Pacific transport of soil dust is controlled by the relative strength and orientation of the major East Asian trough system. The trans-Pacific transport of soil dust and its intrusion to the North American coast show good agreement with ground and aircraft observations in the vicinity of the Olympic Peninsula. Near the source region, simulations suggests that the dust plume peaked to about 2 km above the ground, whereas dust layers could maximize as high as 7 km aloft over the west coast of North America. Sulfate aerosols measured in the Saturna Island (CAPMoN) did not show any significant correlation with the dust component (calcium). Owing to model resolution limitations and treatment of PBL in the NARCM model, the detailed pathway of downward transport of soil dust over the west coast cannot be accurately simulated from the current model. A more sophisticated model with more detailed PBL treatment is recommended to study this phenomenon in future.

[44] **Acknowledgments.** The authors wish to thank the Canadian Climate Research Network (CCRN) and the Canadian Foundation for Climate and Atmospheric Sciences (CFCAS) for their financial support for this research. The authors also wish to thank MOST (grant G2000048703), CAS (grant KZCX2-305), NSF of China (grants 40121303 and 49825105) for support and Qiguo Zhao of Nanjing Soil Institute of Chinese Academy of Sciences for providing the Chinese soil texture map. The initial source code for the dust emission scheme from Marticorena of France is greatly appreciated. We thank Norm O'Neill of CARTEL, University of Sherbrooke, for providing the optical depth data at Saturna Island. Finally, we wish to thank Ki-Hyun Kim of Sejong University, Korea, for providing the elemental compositions of spring 2001 at Seoul.

References

Alfaro, S. C., and L. Gomes, Modeling mineral aerosol production by wind erosion: Emission intensities and aerosol size distribution in source areas, *J. Geophys. Res.*, *106*, 18,075–18,084, 2001.

Alfaro, S. C., A. Gaudichet, L. Gomes, and M. Maillé, Modeling the size distribution of a soil aerosol produced by sandblasting, *J. Geophys. Res.*, *102*, 11,239–11,249, 1997.

Alfaro, S. C., A. Gaudichet, L. Gomes, and M. Maillé, Mineral aerosol production by wind erosion: Aerosol particle sizes and binding energies, *Geophys. Res. Lett.*, *25*, 991–994, 1998.

Balkanski, Y., M. Schulz, B. Marticorena, G. Bergametti, W. Guelle, F. Dulac, C. Moulin, and C. Lambert, Importance of the source term and of the size distribution to model the mineral dust cycle, in *The Impact of Desert Dust Across the Mediterranean*, edited by S. Guerzoni, and R. Chester, pp. 69–76, Kluwer Acad., Norwell, Mass., 1996.

Charlson, R. J., J. E. Lovelock, M. O. Andreae, and S. G. Warren, Oceanic phytonplankton, atmospheric sulphur, cloud albedo and climate, *Nature*, *326*, 655–661, 1987.

Chinese Academy of Sciences, *Chinese Desertification Map*, Resource and Environment Database, Beijing, 1998.

Dickinson, R. E., A. Henderson-Sellers, P. J. Kennedy, and M. F. Wilson, Biosphere-atmosphere transfer scheme (BATS) for the NCAR community climate model, p. 69, Boulder, Colo., 1986.

Duce, R. A., *Sources, Distributions and Fluxes of Mineral Aerosols and Their Relationship to Climate*, pp. 43–72, John Wiley, New York, 1995.

Duce, R. A., C. K. Unni, B. J. Ray, J. M. Prospero, and J. T. Merrill, Long-range atmospheric transport of soil dust from Asia to the tropical North Pacific: Temporal variability, *Science*, *209*, 1522–1524, 1980.

Fécan, F., B. Marticorena, and G. Bergametti, Parameterization of the increase of the aeolian erosion threshold wind friction velocity due to soil moisture for arid and semi-arid areas, *Ann. Geophys.*, *17*, 149–157, 1999.

Gomes, L., G. Bergametti, G. Coudeo-Gaussen, and P. Rognon, Submicron desert dusts: A sandblasting process, *J. Geophys. Res.*, *95*, 13,927–13,935, 1990.

Gong, S. L., et al., Canadian Aerosol Module: A size-segregated simulation of atmospheric aerosol processes for climate and air quality models: 1. Module development, *J. Geophys. Res.*, *108*(D1), 4007, doi:10.1029/2001JD002002, 2003.

Herman, J., P. Bhartia, O. Torres, C. Hsu, C. Seftor, and E. Celarier, Global distribution of UV-absorbing aerosols from Nimbus 7/TOMS data, *J. Geophys. Res.*, *102*, 16,911–16,922, 1997.

Hseung, Y., *The Soil Atlas of China*, Cartographic Publ., Beijing, 1984.

Husar, R. B., J. M. Prospero, and L. L. Stowe, Characterization of tropospheric aerosols over the oceans with the NOAA advanced very high resolution radiometer optical thickness operational product, *J. Geophys. Res.*, *102*, 16,889–16,909, 1997.

Husar, R. B., et al., Asian dust events of April 1998, *J. Geophys. Res.*, *106*, 18,317–18,330, 2001.

Jaffe, D. A., et al., Transport of Asian air pollution to North America, *Geophys. Res. Lett.*, *26*, 711–714, 1999.

Laymon, C., W. Crosson, T. Jackson, A. Manu, and T. Tsegaye, Ground-based passive microwave remote sensing observations of soil moisture at S-band and L-band with insight into measurement accuracy, *IEEE Trans. Geosci. Remote Sens.*, *39*(9), 1844–1858, 2001.

Marticorena, B., and G. Bergametti, Modeling the atmospheric dust cycle: 1. Design of a soil-derived dust emission scheme, *J. Geophys. Res.*, *100*, 16,415–16,430, 1995.

Marticorena, B., G. Bergametti, and B. Aumont, Modeling the atmospheric dust cycle: 2. Simulation of Saharan dust sources, *J. Geophys. Res.*, *102*, 4387–4404, 1997.

Martin, J. C., et al., Testing the iron hypothesis in ecosystems of the equatorial Pacific Ocean, *Nature*, *371*, 123–129, 1994.

Overpeck, J., D. Rind, A. Lacis, and R. Healy, Possible role of dust-induced regional warming in abrupt climate change during the last glacial period, *Nature*, *384*, 447–449, 1996.

Pielke, R. A., *Mesoscale Meteorological Modeling*, 612 pp., Academic, San Diego, Calif., 1984.

Prospero, J. M., and D. L. Savoie, Effect of continental sources of nitrate concentrations over the Pacific Ocean, *Nature*, *339*, 687–689, 1989.

Robert, A., T. L. Yee, and H. Ritchie, A semi-Lagrangian and semi-implicit numerical integration scheme for multilevel atmospheric models, *Mon. Weather Rev.*, *133*, 388–394, 1985.

Sokolik, I. N., and O. B. Toon, Direct radiative forcing by anthropogenic airborne mineral aerosols, *Nature*, *381*, 681–683, 1996.

Sokolik, I. N., D. M. Winker, G. Bergametti, D. A. Gillette, G. Carmichael, Y. J. Kaufman, L. Gomes, L. Schuetz, and J. E. Penner, Introduction to special section on mineral dust: Outstanding problems in quantifying the radiative impacts of mineral dust, *J. Geophys. Res.*, *106*, 18,015–18,027, 2001.

Song, C. H., and G. Carmichael, A three-dimensional modeling investigation of the evolution processes of dust and sea-salt particles in East Asia, *J. Geophys. Res.*, *106*, 18,131–18,154, 2001.

Taylor, P., Comments and further analysis on the effective roughness length for use in numerical three dimensional models, *Boundary Layer Meteorol.*, *39*, 403–419, 1987.

Tegen, I., and I. Fung, Modeling of mineral dust in the atmosphere: Sources, transport, and optical thickness, *J. Geophys. Res.*, *99*, 22,897–22,914, 1994.
Thulasiraman, S., N. T. O'Neill, A. Royer, B. N. Holben, D. Westphal, and L. J. B. McArthur, Sunphotometric observations of the 2001 Asian dust storm over Canada and the U.S., *Geophys. Res. Lett.*, *29*(8), doi:10.1029/2001GL014188, 2002.
Uematsu, M., R. A. Duce, J. M. Prospero, L. Chen, J. T. Merrill, and R. L. McDonald, Transport of mineral aerosol from Asia over the North Pacific Ocean, *J. Geophys. Res.*, *88*, 5343–5352, 1983.
Uno, I., H. Amano, S. Emori, N. Kinoshita, I. Matsu, and N. Sugimoto, Trans-Pacofic yellow sand transport observed in April 1998: Numerical simulation, *J. Geophys. Res.*, *106*, 18,331–18,344, 2001.
Verseghy, D. L., CLASS—A Canadian land surface scheme for GCMS, I, Soil model, *Int. J. Climatol.*, *11*(2), 111–133, 1991.
Wang, Z., H. Ueda, and M. Huang, A deflation module for use in modeling long-range transport of yellow sand over East Asia, *J. Geophys. Res.*, *105*, 26,947–26,959, 2000.
Webb, R. S., C. E. Rosenzweig, and E. R. Levine, A global data set of soil particle size properties, *NASA Tech. Memo.*, *4286*, 34 pp., 1991.
Zhang, D. E., Synoptic-climatic studies of dust fall in China since the historic times, *Sci. Sin.*, *27*(8), 825–836, 1984.
Zhang, L., S.-L. Gong, J. Padro, and L. Barrie, A size-segregated particle dry deposition scheme for an atmospheric aerosol module, *Atmos. Environ.*, *35*(3), 549–560, 2001.
Zhang, X. Y., S. L. Gong, Z. X. Shen, F. M. Mei, X. X. Xi, L. C. Liu, Z. J. Zhou, D. Wang, Y. Q. Wang, and Y. Cheng, Characterization of soil dust aerosol in China and its transport and distribution during 2001 ACE-Asia: Network observations, *J. Geophys. Res.*, *108*, doi:10.1029/2002JD002632, in press, 2003.
Zobler, L., A world soil file for global climate modeling, *NASA Tech. Memo.*, *87802*, 33 pp., 1986.

S. L. Gong, Air Quality Research Branch, Meteorological Service of Canada, 4905 Dufferin Street, Toronto, Ontario, Canada M3H 5T4. (sunling.gong@ec.gc.ca)

D. A. Jaffe, University of Washington-Bothell, 18115 Campus Way NE, Bothell, WA 98011-8246, USA.

N. M. Lu, National Satellite and Meteorological Center, Chinese Meteorological Administration, Number 46, Baishiqiao Road, Beijing 100081, China.

I. G. McKendry, Atmospheric Science Programme/Geography, University of British Columbia, 251-1984 West Mall, Vancouver, British Columbia, Canada.

X. Y. Zhang, Stake Key Laboratory of Loess and Quaternary Geology, Institute of Earth Environment, Chinese Academy of Sciences, P.O. Box 17, Xian 710075, China.

T. L. Zhao, Department of Chemical Engineering and Applied Chemistry, University of Toronto, Toronto, Ontario, Canada M5S 3E5.